Progress Report 2011 and Beam Request for 2012

Muon Capture on the Deuteron

The MuSun Experiment

PSI Experiment R-08-01, spokespersons P. Kammel, C. Petitjean, A.A. Vasilyev

MuSun Collaboration [1]

Petersburg Nuclear Physics Institute – University of Washington Seattle – Paul Scherrer Institut – University of Kentucky – Boston University – Regis University – University of South Carolina– Université Catholique de Louvain

http://muon.npl.washington.edu/exp/MuSun

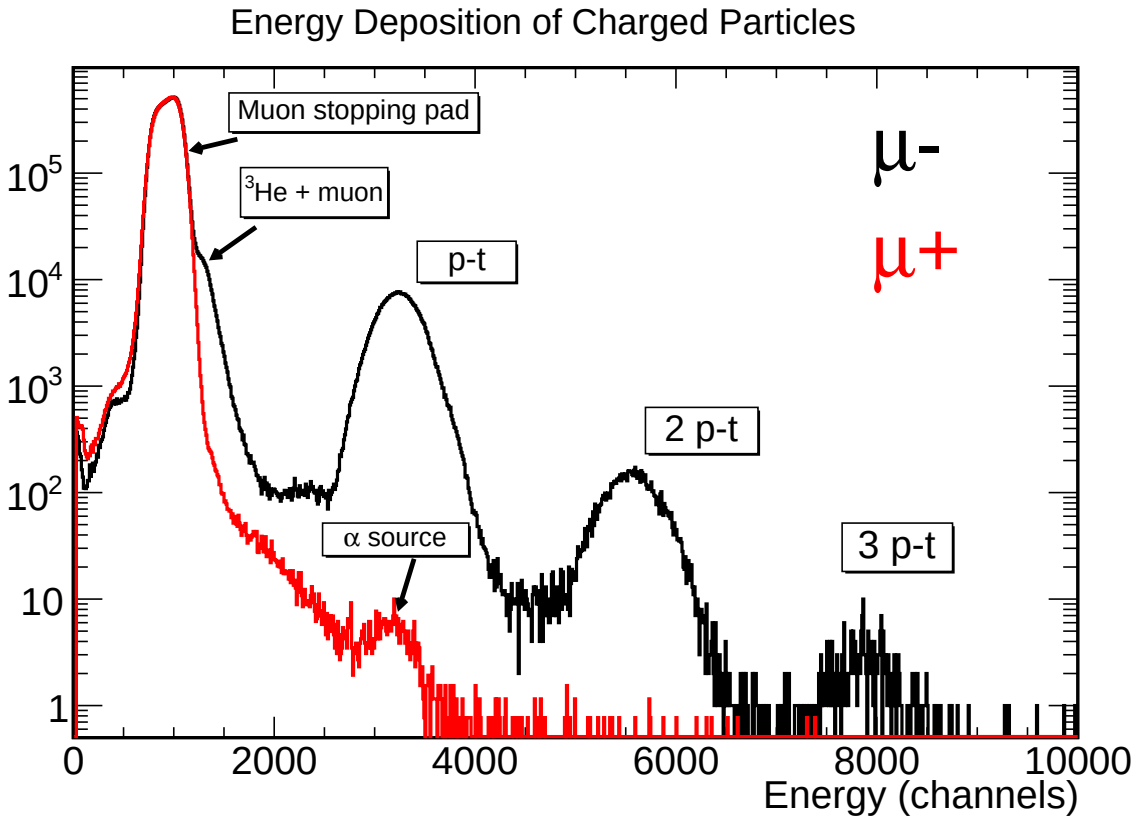

Figure 1: Energy of charged particles in the CryoTPC. Negative muons produce the ^{3}He and p-t fusion products.

Contents

1 Overview **3**
- 1.1 Physics Update and Experimental Strategy . . . 3
- 1.2 Highlights 2011 . . . 4
  - 1.2.1 Run R2011 June-Sept 2011 . . . 4
  - 1.2.2 πE1 beam test Oct-Nov 2011. . . . 5

2 Run 2011 Overview **5**

3 System Status and Performance **6**
- 3.1 Front End Electronics . . . 6
- 3.2 DAQ . . . 7
- 3.3 Beam . . . 8
- 3.4 TPC and Cryosystem . . . 9
- 3.5 μSR magnet . . . 11
- 3.6 Electron Detectors . . . 12
- 3.7 Neutron Detectors . . . 12
- 3.8 Ge and NaI detector . . . 13

4 Analysis Roadmap **14**
- 4.1 Analysis Framework . . . 15
- 4.2 Basic Analyses . . . 16
  - 4.2.1 TPC and Muon Stop . . . 16
  - 4.2.2 Electron time spectra . . . 19
  - 4.2.3 Neutrons and X-ray detection . . . 20
- 4.3 Systematic and Optimization Studies . . . 23
  - 4.3.1 Fusion interference . . . 23
  - 4.3.2 TPC purity . . . 24
- 4.4 Monte Carlo . . . 26

5 Plans and Beam Time Request 2012 **28**
- 5.1 Development of expanded πE3 area . . . 28
- 5.2 Collaboration Plans and Tasks . . . 29
  - 5.2.1 Tasks and upgrades before the run . . . 29
  - 5.2.2 Run Plan . . . 31
- 5.3 Beam Time Request . . . 31

1 Overview

1.1 Physics Update and Experimental Strategy

We are now at the confluence of two exciting developments in the field of muon capture [2]. Based on the novel "active target" technique developed by our collaboration, experiments on hydrogen and the lightest nuclei are approaching sub-percent precision, surpassing the precision of previous generations of experiments by about an order of magnitude. At the same time, following Weinberg's pioneering approach, effective field theories (EFTs) have been systematically constructed to calculate electro-weak observables in few-body systems. Thus simple nuclear systems become amenable to rigorous QCD-based calculations. On the one hand, these calculations can provide precise results, including a systematic evaluation of their uncertainties. On the other hand, they can establish quantitative relations between muon capture and electro-weak astrophysical processes of fundamental importance, which have never been measured directly. These include pp fusion, which is the primary energy source in the sun and the main sequence stars, and the νd reaction, which provided convincing evidence for solar neutrino oscillations at the Sudbury Neutrino Observatory.

The prime example is the process

$$\mu + d \rightarrow n + n + \nu \tag{1}$$

which is the simplest muon capture process on a nucleus. The basic pseudoscalar coupling g_P required for such calculations has been measured by the MuCap experiment. In modern calculations of the capture rate Λ_d for process (1), the standard nuclear physics approach (SNPA), based on the impulse approximation with explicit modeling of two-body current contributions, is being replaced by less model-dependent hybrid EFT calculations; a pion-less EFT calculation has also been performed. Results since 2000 are compiled in table 1. The prospect for a precise MuSun result has stimulated recent calculations. 2011 saw an exciting development in the long history of this field, as first steps towards a fully self-consistent EFT treatment were taken. The new development overcomes the consistency issue in hybrid EFT, where operators are derived from EFT, but wave functions are calculated from phenomenological potentials. These new results are still unpublished and need further scrutiny, but they already document significant advances on the theory side [3]. With the planned precise MuSun result, the sole unknown low-energy constant (LEC), $\hat{d}_R$ or c_D, involved in an EFT calculation of the pp-fusion rate can be determined purely within two-nucleon systems. This LEC is also important in the following context. The existing hybrid EFT calculations use the tritium beta-decay rate to control Λ_d, but it is known that the use of three-nucleon (3N) systems introduces a second LEC in the 3N forces. This point is masked in a hybrid EFT treatment that adopts phenomenological potentials. It is expected that a fully consistent EFT calculation extended to 3N systems will be able to address this issue in the future.

While μd capture could serve as the benchmark for the axial current interaction in the two-nucleon system, the present experimental situation is inadequate to provide much guidance. The best existing experiments [4, 5] are not precise enough and the most precise result differs from modern theory by three standard deviations. If true, such a discrepancy would have major ramifications for the above-mentioned astrophysics processes.

The goal of the MuSun experiment is the measurement of the rate Λ_d to a precision of better than 1.5%. Λ_d denotes the capture rate from the doublet hyperfine state of the muonic deuterium atom in its 1S ground state. This measurement will clarify the current tension between experiment and theory and provide a benchmark commensurate with the expected precision of ongoing, modern calculations. For the foreseeable future, the MuSun experiment is the only theoretically clean way to determine the important axial low-energy constant,

Λ_d	year	Method	Reference
386	2001	EFT*	Ando, Phys. Lett. B533, 25-36
416±6	2009	SNPA, EFT*	Ricci, Nucl. Phys. A837, 110
392.0±2.3	2011	EFT*	Marcucci, Phys.Rev.C83:014002
399.0±3	2011	EFT	Marcucci, arXiv:1109.5563 [nucl-th]
410-417	2011	EFT	Adam, arXiv:1110.3183 [nucl-th]

Table 1: Recent theoretical results on muon capture rate Λ_d from the doublet state of the μd atom. EFT* denotes a hybrid EFT calculation. The pion-less EFT calculation [6] cannot be expressed by a single value and therefore is not included in the table. The last two lines refer to the very recent full EFT calculations.

which is required for calculating both μd capture as well as pp fusion and νd scattering. The anticipated precision is 5 times greater than presently available from the 2N system and will be essential for calibrating these reactions in a model-independent way.

The MuSun experiment is built on the MuLan and MuCap techniques developed at PSI. Like MuCap, it is a measurement of the negative muon lifetime in a gaseous tracking chamber. The experiment must be performed under conditions such that Λ_d can be extracted unambiguously, independent of muonic atomic physics complications occurring after the muon stops in deuterium. The transition between the upper μd quartet to the lower μd hyperfine state is slow and, once a $dd\mu$ molecule is formed, muon-catalyzed dd fusion occurs within nanoseconds. Our studies demonstrated that atomic physics uncertainties are reduced to a negligible level at optimized target conditions of T = 30 K and 6% liquid hydrogen density. To achieve such conditions, a new high-density cryogenic ionization chamber filled with ultra-pure deuterium has been developed. This Time Projection Chamber (TPC) must define the muon stop, identify impurities, and observe muon-catalyzed reactions. It must have very good energy resolution and full analog readout using flash ADCs. This information is critical to avoid systematic uncertainties in the muon stop definition and to detect the charged particles induced by the fusion and impurity capture processes. Since the target density of MuSun is five times higher than that of MuCap, the chamber does not have internal gas gain and drift voltages up to 80 kV are required.

1.2 Highlights 2011

1.2.1 Run R2011 June-Sept 2011

A 12-week data production run, using the well-tuned, high-quality $\pi E3$ beam for the last time, was the highlight of last year. Key preparatory tasks included: i) Generation of 1500 l atmospheric liters of isotopically pure deuterium (protium < 40 ppm), which was a limiting factor during 2010 running. ii) Significant improvements in TPC resolution and sparking. iii) Improved pad plane and non-magnetic grid frame in the TPC. Many other subsystems were enhanced as well and, as additional monitoring devices, X-ray detectors were installed. These developments led to a first production run, with the complex detector and cryogenic infrastructure working reliably. A data set of about 5 10^9 fully-reconstructed negative muon decays was collected. To aid our understanding of the TPC, a number of detailed systematic studies were performed, over a wide range of operating conditions. The collaboration was strengthened by a new PhD student and two new postdocs, who worked at PSI for the first time. It also provided an exciting learning experience for five undergraduate students, two of whom were supported by PSI. We are confident that the ongoing analysis of this data will lead to a first physics result from the MuSun experiment. It will also provide guidance for detector upgrades, as we prepare for experimental running in the new, extended πE1 area.

1.2.2 πE1 beam test Oct-Nov 2011.

In October and November, a PSI team (A. Antognini et al.) conducted a separate, low energy muon beam test in the old, constricted πE1 area. Their two goals were to develop an ultra-low energy muon beam and to test muon cooling methods. Part of this beam time was devoted to evaluating the phase space and intensity of 30-40 MeV/c muons, in a beamline configuration equivalent to that of an extended πE1: (hor. separator - quad-doublet - slit - quad-doublet). The beam scintillator telescope (μSC, μSC-A: slab with central hole, 35 mm diameter) and the vacuum nose from MuSun were used for these measurements. At beam momentum 35 MeV/c, with momentum slits open and a primary proton beam current of 2.15 mA, a flux of 145 kHz of high quality μ^- was observed in counter μSC, while counter μSC-A registered 82 kHz. Scaled to MuSun's nominal momentum 40 MeV/c, the measured fluxes correspond to 230 kHz (μSC) and 130 kHz (μSC-A) , which is promising news. Of course, a conclusive assessment cannot be given until beam tests are performed in the expanded πE1 area.

2 Run 2011 Overview

The first few weeks in the summer of 2011 were spent preparing the various detector and data acquisition systems for the upcoming data-taking period. Activities were centered around assembling and testing the cryogenic TPC, upgrading the electronics of the two electron wire chambers (ePC1 and ePC2) and preparing the read-out electronics for the TPC.

A number of modifications were made to the TPC, including four new field-shaping wires, new MACOR supports and a new anode pad plane (Sect. 3.4). The preliminary work on the electron wire chambers consisted of a series of noise studies and the replacement of the amplifier-discriminator cards for the cathode strips with redesigned ones (Sect. 3.6). Further noise studies were also done on the waveform digitizers used to read out the TPC (Sect. 3.1).

When the collaboration gained access to the $\pi E3$ area, the different detector systems were assembled and the necessary beamline elements were put in place (Sect. 3.3). At the same time, the online analysis software was updated with the latest developments from the offline and new displays were implemented. Production data-taking started at the beginning of July. To maintain an unbiased analysis, the master clock frequency was set by a PSI scientist who is not involved in the analysis. The display of the synthesizer was then covered up but checked weekly by that same scientist. Although the frequency is known to be 498.5 MHz $< f_{Run2011} <$ 499.5 MHz, its exact value will remain hidden until the analysis is complete.

The first two weeks of production data taking saw the installation of the μSR magnet (Sect. 3.5) and its negative effect on the gain of the neutron detectors (Sect. 3.7). After the installation of magnetic shields, smooth and stable data-taking followed. μ^+ data was taken for a few days before the planned beam shutdown around the beginning of August. During shutdown, a muonic X-ray detector was installed (Sect. 3.8).

Once μ^- production data-taking resumed, some problems appeared. The muonic X-ray detectors affected other detector systems. The entrance wire chamber (μPC) saw an increase of single-plane hits. At the same time, the waveform digitizers used to read out electron scintillators would suffer sporadic losses of data. Recabling and regrounding of the muonic X-ray detector helped restore normal data-taking.

Additionally, various systematic data sets were obtained. To help with the background analysis and electron wire chamber alignment, a small set of cosmic ray data was recorded. To better understand the effect of electron attachment and impurities on the signals (Sect. 4.3.2), data was taken with the TPC operating at different densities and temperatures.

The R2011 run produced a total of 31.6 terabytes (TB) of data. Roughly 23.7 TB passed an

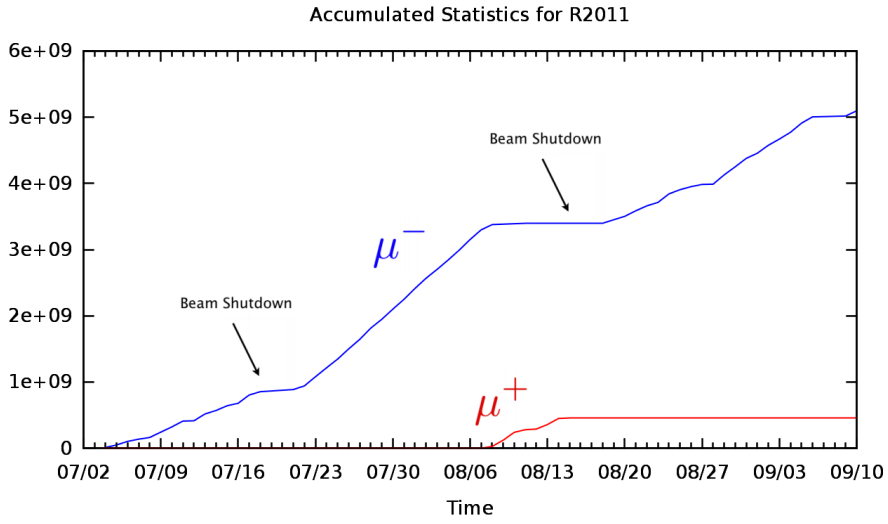

Figure 2: Accumulated statistics (muon and decay electron pairs for μ^- (blue) and μ^+ (red)). The lower *good* data rate after the second beam shutdown was due to the increase of noise in the μPC, but we are confident this can be recovered in the off-line analysis.

initial quality check, with 21.2 TB corresponding to μ^- events and 2.5 TB to μ^+. Scintillation counters placed at the end of the beamline registered approximately 3.4×10^6 pileup-protected muons entering the TPC per data file (around 3 minutes of data taking). An initial analysis of the data reveals roughly 5.2×10^9 muon-electron pairs: good muons stops in the TPC accompanied by fully reconstructed decay-electron tracks, including 4-fold coincidences in the gondola scintillator detectors (Fig.2).

3 System Status and Performance

3.1 Front End Electronics

The two ePCs are read out through the Louvain compressor boards. The scintillator detectors, μSC, and eSC are read out in a traditional manner with discriminators and multihit TDCs, and also with 500 MHz waveform digitizers(WFDs). Those signals consist of 48 samples framed around the peak. The signals from the TPC preamplifiers and shaping amplifiers are recorded with the same WFDs, sampling at 25 MHz. Typical waveforms, WFD *islands*, consist of 88 samples, including 25 presamples from the region before the trigger signal. To allow for pulse shape discrimination, using both the peak and tail of the pulse, the liquid-scintillator neutron detectors need a large dynamic range. The high-purity germanium and sodium iodide detectors, used to detect muonic X rays require excellent energy resolution. Both the neutron and X-ray detectors were connected to 12-bit, 170 MSPS waveform digitizers, *FADCs*, that were originally developed by the Berkeley and Louvain groups for the MuCap experiment.

The electronic noise of the TPC signals has an RMS width of 1 or 2 ADC counts in the WFDs (equivalent to 18-36 keV energy deposition). In earlier runs, the operation of the cold head produced significant acoustic vibration, which was picked up by the signals. For the 2011 run, each channel of the shaping amplifiers was equipped with a baseline restorer. As a result, the acoustic noise was greatly reduced, increasing the energy resolution by factor of 1.5 (Fig. 3). Many channels also display what looks like intermittent high frequency switching noise, but for which the origin remains obscure. The noise is only observed in the experimental hall. When it falls on top of real signals, our pulse fitting procedures can filter out the high

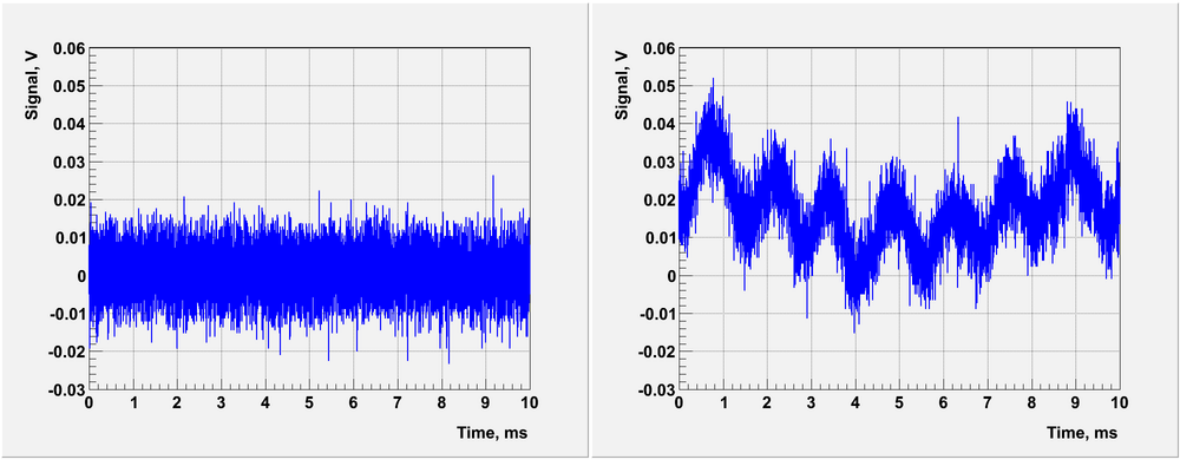

Figure 3: The effect of the baseline restorers is evident. The right picture shows the acoustic noise of one channel of the TPC, without the baseline restorer, measured with the oscilloscope. The left picture shows the same channel with the baseline restorer turned on.

frequency noise with little effect on the χ^2.

The Boston group has developed more sophisticated firmware to address the effect of noise on the trigger, without changing the signal itself. The effect of any remaining acoustic noise is minimized by running the samples through a real-time digital filter, which removes any oscillations in the frequency region from 1-7000 Hz. The trigger can then be established with respect to this filtered baseline. The new firmware can also run with an integral threshold, so that readout is triggered on the average value of a number of samples (above some background) rather than on an individual sample. This new *smart* trigger was deployed on a special TPC WFD module, which read out extra copies of several pad signals.

3.2 DAQ

The general structure of the data acquisition system (DAQ) remained similar to that of the previous year. Since 2011 was the first production year for MuSun, the primary efforts were focused on ensuring smooth data taking and good data quality. Modifications included *i)* a new approach to data storage, *ii)* improvements to the online data monitoring system, *iii)* an upgrade to the offline data analysis system.

In 2011, we replaced the tape-based data archiving system with a new approach based on hard disks. Two hot-swappable 2TB hard disk cradles were connected to the backend PC over an eSATA interface. The lazy logger writes the data on one hard disk and rotates the disks automatically when the active disk is full. All disks are uniquely labeled and numbered during file system formatting. On disk rotation, the disk number is incremented automatically and checked against the hard disk label to ensure that the data will be written to the right medium. Thus, the system requires minimal attention from shift personnel. The archived data from the 2 TB hard disks was copied over the network to mass storage at the Lonestar facility in Texas, using a standalone PC equipped with a similar hard disk cradle.

The online and offline data analysis and monitoring systems were essential to ensure good quality of the production data. A significant effort was made to merge the online and the offline analyzer programs. To monitor data quality, the same analyzer code can now be used online, on small fractions of the data or offline, on larger data sets. The off-line analysis capability was upgraded with three computers based on new generation Intel® Core™ i7 CPUs. Twelve CPU cores can be used to analyze twelve runs in parallel.

The primary MuSun server, which provides Web, MySQL, TFTP and NFS services for the experiment including remote file systems for diskless frontend computers, was also upgraded. The new PC uses two hard disks combined into a Redundant Array of Independent Disks (RAID1) to minimize the probability of downtimes caused by potential disk failures.

3.3 Beam

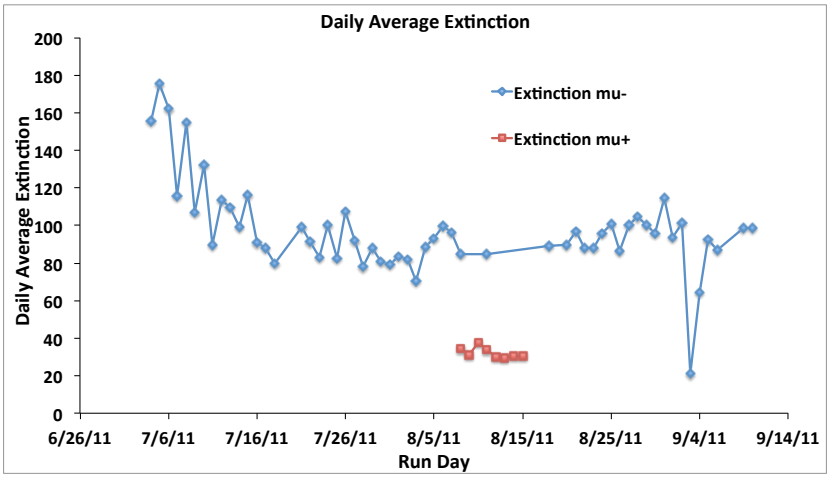

Figure 4: The daily average extinction measured throughout R2011. The blue line is for μ^- data and the red is for μ^+ data. There was a drop in the average extinction on the 16^{th} of July when we attempted to increase the μ^- rate. The low extinction observed on the 3^{rd} and 4^{th} of September can be attributed to problems with the kicker, which were later resolved.

The MuSun 2011 production run consisted of 12 weeks of beam time (June 20 to September 12) in the πE3 area. The MuSun beamline design includes a vertical separator and the MuLan kicker. Two different tunes were employed, one for μ^- runs and one for μ^+ runs. In addition, slit3 aperture and the separator current were both increased when the MEG experiment's COBRA magnet was powered. The main addition to the 2010 MuSun beamline was a steering magnet situated downstream of the beamline, before the entrance detectors. With the help of the steering magnet, which was used to offset the beam horizontally by 1 cm, the beamspot is centered in both X and Y (Fig. 5).

Detectors	**Rate (kHz)**
μSC entrance scintillator (raw)	24.3
Full pile-up protected μSC and μPC (Good muon entrance)	17.8
Good Muon entrances that stop in TPC fiducial volume	5.6
Good Muon entrances that stop in TPC fiducial volume and have an electron track	3.0

Table 2: Table displaying the muon rates at various locations throughout the MuSun experiment, based on an average from a selection of production data throughout R2011. The μSC and μPC are entrance detectors. Good muon entrances have no pile-up with other muons. The current TPC stop is defined as a muon track with signals on at least 3 pads in a row, the fiducial cut is a horizontal veto on the border pads, and a vertical veto up to 16 mm from the anode and cathode planes.

The nominal momentum setting for $\mu^-(\mu^+)$ data-taking was 40.3 MeV/c(40.6 MeV/c).

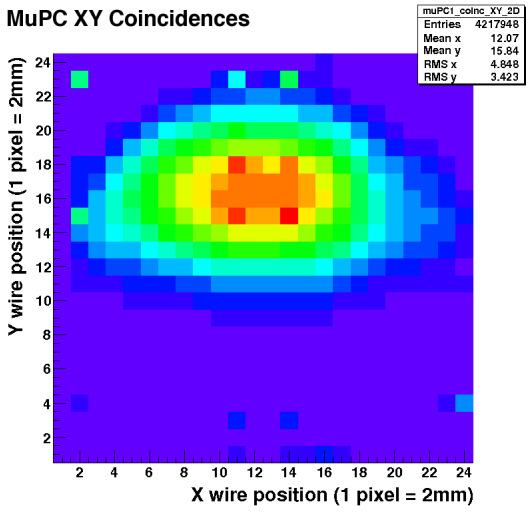

Figure 5: The x and y co-ordinates of the beamspot as measured by the MuPC entrance detector. 1 pixel on the figure is equivalent to 2 mm. Before the implementation of the steering magnet there was a 1 cm offset in the horizontal direction.

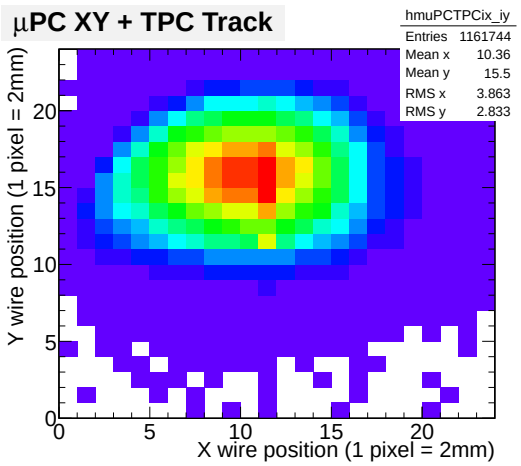

Figure 6: A coincidence requirement with the TPC does not change the shape, indicating that the beam passes cleanly through the entrance window.

A negative muon rate of 25 kHz (with the kicker operational) with an extinction of ∼90 was achieved. For positive muons the rate was ∼30 kHz (with the kicker operational) with an extinction of ∼35. The daily average extinction throughout the run is shown in Fig. 4. For μ^- data, a breakdown of the muon rates at various locations throughout the MuSun experiment is shown in Table 2. About 12 % of the muons that enter the MuSC entrance detector end up in the final statistics of Fig. 2. The proton beam was relatively stable throughout the run, reaching 2.3 mA at times. However, when hot weather brought beamline cooling issues, the beam current was reduced to 1.7 mA , with a resulting drop in the muon rate from ∼25 kHz to ∼21 kHz. The experiment was live for 31.6 of the 56 days of μ^- data taking and 3.9 of the 10 days of μ^+ data taking.

3.4 TPC and Cryosystem

The basic design of the CryoTPC system was unchanged but some of its subsystems were upgraded. The stability of the high voltage system was improved and both acoustic and electronic noise were reduced. In addition, considerable care was taken to improve the chamber's reliablity as well as its chemical purity. The configuration of the CryoTPC is shown in Fig. 7.

A new **cathode plane**, laminated with a 100 μm layer of silver, was installed. This thin layer of high-Z material diminishes the effect on the muon lifetime by muons stopped in the cathode, since the lifetime of muonic silver atoms is only 87 ns. The cathode plane operated stably at 80 kV during the entire run.

A new **anode plane** was manufactured from MACOR, with chemically-deposited gold-plated pads. A new set of flat Kapton signal cables was made as well. The advantages of the new "pad plane + cables" assembly include a considerable reduction in out-gassing and the short life time of errant muons which stop in the Au pad plane.

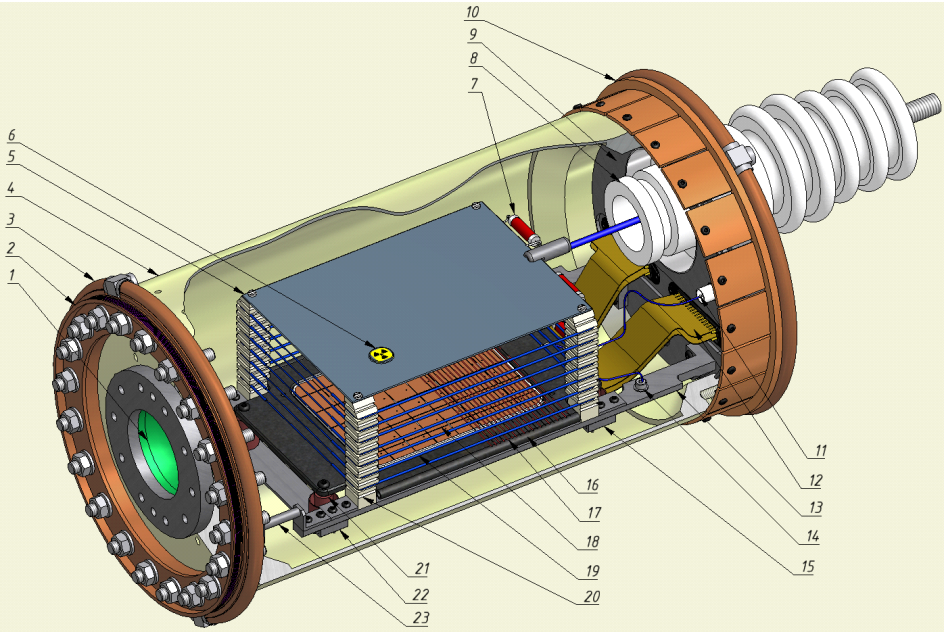

Figure 7: CryoTPC layout. 1 - beryllium window, 2 - heater, 3, 10 - heat exchangers, 4 - shell, 5 - cathode, 6 - α source, 7 - dividing resistor, 8 - cathode HV feedthrough, 9 - main flange, 11 - anode HV feedthrough, 12 - flat signal cable, 13 - support, 14 - grounding terminal, 15, 22 - brackets, 16 - shielding grid frame, 17 - grid, 18 - anode (pad plane), 19 - field-shaping wires, 20 - MACOR stand, 21 - grid insulator, 23 - guide

The new ***Frisch* grid** is made entirely from austenite stainless steel, which excludes effects of temperature deformations. A set of measurements was carried out at PNPI to determine the type of steel with minimal magnetic susceptibility. During the entire run, the grid operated stably at 3500 kV, the maximum high voltage that could be set without sparking to the anode plane.

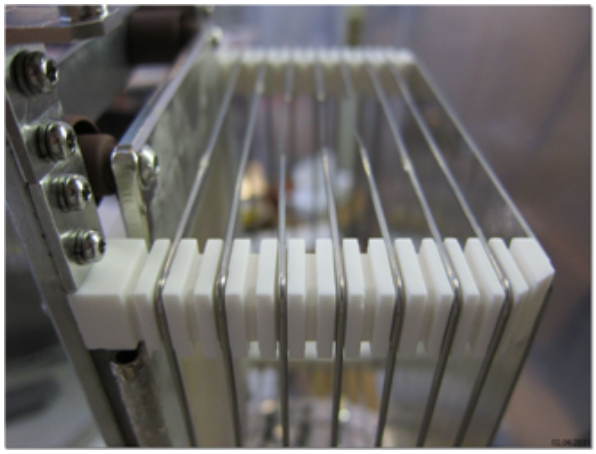

Figure 8: The field-shaping wires with their MACOR support rods. The middle wires at the upstream side of the TPC have a reduced thickness to minimize μ scattering.

To improve the rigidity of the TPC, a new set of **field-shaping wires** was made. The new, monolithic MACOR support stands (Fig. 8), are more reliable than the previous design.

By increasing the number of crosscut grooves and a better surface quality, the electrical insulation properties of the stands were improved as well.

The **cryogenic system** (Fig. 19 in [7]) was reassembled with tighter connections, eliminating neon leaks to the vacuum volume of the system. The cryogenic system remained stable throughout the run, without any interruption. Because of a small heat leak somewhere in the neon lines, however, TPC operation was restricted to 34 K or higher. The absolute temperature calibration was done by measuring the saturated vapor pressure curve of deuterium in the working temperature range (34-75 K).

A **gas storage volume**, with an inner volume of 250 liters and 15 bar of working pressure, was built to store the entire gas reserve between major data-taking runs. To help maintain the chemical purity of the deuterium gas, the new vessel is made of stainless steel. The storage volume is equipped with heat insulation, temperature control and a vacuum port to allow high vacuum pumping accompanied by continuous baking. This treatment removes water which adheres to the vessel's inner surface and, as a result, minimizes hydrogen contamination in the deuterium. During the run, the gas holder is installed in the gas circuit and serves as an additional reserve and safety release buffer.

As a **safety upgrade**, an extra high pressure release valve to outside for the D_2 gas was installed during the run. In addition, a subsystem to protect against overheating during the warming procedure was added to the control system.

3.5 μSR magnet

Some fraction of the μ^+ stopped in the TPC will retain their initial polarization. Precession in ambient magnetic fields and depolarization of these muons during the measurement period can result in a systematic error in the lifetime measurement. In order to control the precession, a $\sim$50 gauss magnetic field was applied to the fiducial volume, transverse to the beam axis. As a result, the exponential lifetime spectrum of the μ^+ will be modulated by a sinusoidal muon spin-rotation (μSR) signal. This signal, dominated by the "free" μ^+ in the deuterium gas [8], can be enhanced by taking the difference of signals for two opposing segments of the electron detector. In order to maintain stable experimental conditions, and to eliminate[1] a μSR signal from a possible remnant polarization of the $\mu^- d$ atoms, the μSR magnetic field was left on during the entire run. The μSR magnet is a paired saddle-coil magnet which is located outside the outer TPC vessel. To minimize scattering of decay electrons, the windings were made as light as possible. Each pair consists of eight hollow aluminum tube windings, with cooling water flowing through them. A current of 125 A generates a relatively uniform magnetic field of 50 gauss in the fiducial volume of the TPC.

A 160 mH magnet and a 40 mF capacitor serve as inductive and capacitive filters, respectively, for the μSR magnet's power supply. As a safety feature, the power supply was interlocked with the water pump providing the cooling water, and PT100 temperature sensors were placed on both magnets. In addition, two Hall probes, a humidity sensor, and four temperature sensors, placed at different places on and around the magnet, were read out by the DAQ's slow control. The μSR magnet's stray field had a severe effect on the gain of the neutron detectors, requiring addition shielding efforts (Sect. 3.7). No interference of the stray field with any of the other detector systems were observed.

[1] The precession frequency for the quartet state is 2GHz for a 50 G external magnetic field

3.6 Electron Detectors

The muon decay electrons are detected with a cylindrical hodoscope consisting of a double layer of scintillator paddles for good timing resolution and two multi-wire proportional chambers for tracking. Signals in the scintillator photomultiplier tubes are read out with waveform digitizers as well as discriminators and multihit TDCs. In both cases, the threshold is set to minimize the effect of small gain variations. Since the gains of several PMTs drifted by as much as a few percent during the production run, the voltages were periodically adjusted so as to balance the amplitude spectra. The photomultiplier tubes are old, and many show significant afterpulsing. Over the course of the run, several PMTs had to be replaced with spares of the same model and age. Because we require a multi-detector coincidence, however, the number of false electron signals resulting from these afterpulses is negligible.

The two wire chambers each consist of an anode plane sandwiched between two cathode planes. The anode wires run along the beam direction and the cathode strips are wound about them with a pitch of $\pm$ 45 degree such that a coincidence determines the interaction point unambiguously. Each of the 2560 channels is read out through a threshold discriminator and time-to-digital converter (TDC). The amplifier-discriminator cards for the cathode strips, mounted on the chamber, pick up noise from the switching power supply of the TDC modules. Additionally, both the amplifiers and logic signal driver had a tendency to oscillate, obliterating the signal. While this was a constant problem in previous runs, a redesign of the cards and a dedicated diagnostic effort in June 2011 ameliorated the problem for the data run last summer.

The reconstruction of the decay electron track and its extrapolation back to the muon stop position require the alignment of both chambers. The three planes of each wire chamber were internally aligned using the decay electron signals themselves. For the relative alignment between the two wire chambers, throughgoing cosmic ray signals were used. Tracks were reconstructed for each wire chamber and the relative offset of the other, in ϕ and z, was obtained by comparing the predicted point of interaction from the track with the data. Finally, both wire chambers were brought into alignment with the scintillator hodoscope, also using cosmic ray signals.

At the beginning of the run, a broken anode wire was identified in the outer chamber; to keep the broken wire at ground potential, three (of 32) sections of the chamber were not brought to high voltage. The remaining 90% of the chamber was operated normally, though this larger chamber showed a few inefficient regions, consisting of sparking single wires, whole cathode or anode cards, and a section apparently unassociated with specific electronic channels. The smaller inner wire chamber was much better behaved, with no particularly inefficient sections.

3.7 Neutron Detectors

Muons in deuterium produce two sources of neutrons: (i) fusion neutrons following $dd\mu$ molecule formation and the subsequent $dd\mu \rightarrow^3 He + n + \mu$ fusion reaction, and (ii) capture neutrons following the $\mu d \rightarrow n + n + \nu$ capture reaction from the muonic deuterium $F = 1/2,\ 3/2$ hyperfine states. The $d\mu d$ fusion neutrons are mono-energetic with energy 2.45 MeV. The two coincident capture neutrons have a continuous energy spectrum that peaks at 1-3 MeV and extends to 53 MeV.

Encoded in the time dependence of the fusion neutrons are the two $dd\mu$ molecular formation rates from the $F = 1/2,\ 3/2$ hyperfine states (λ_q and λ_d) and the hyperfine transition rate (λ_{qd}) from the higher-energy $F = 3/2$ state to the lower-energy $F = 1/2$ state. Consequently, the detection of fusion neutrons will enable the determination of the kinetic parameters λ_{qd},

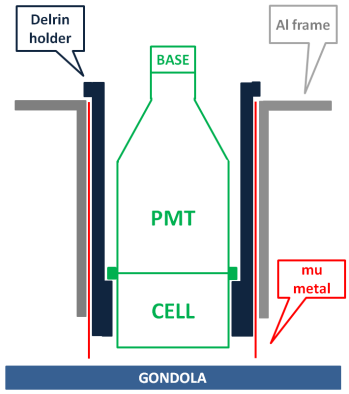

Figure 9: A single mu metal sheet around the PMT and scintillator cell, extending up to the "Gondola" e^- scintillator detector, provided optimal shielding against the stray field of the μSR magnet.

λ_q and λ_d, which are important in the extraction of the μd doublet capture rate, Λ_d, from the measured decay-electron time spectrum.

The detection of μd capture neutrons is more challenging due to their low yield of roughly 10^{-3} per muon stop and their low energies. However, the time spectrum of μd capture neutrons offer the possibility of both a cross-check of the muon induced kinetics and an estimate of the hyperfine capture ratio (*i.e.* the ratio between the μd capture rates from the quartet state Λ_q and the doublet state Λ_d).

The MuSun neutron detection system consists of an eight-detector array with liquid scintillator cells coupled to 13 cm diameter photo-multiplier tubes, read out by an eight-channel 12-bit 170 MHz custom-built waveform digitizers.

Stray magnetic fields of 2-5 gauss from the μSR magnet reduced the gain of the neutron counters by a factor of $\sim$4. The PMT gains were restored by shielding the counters with sheets of mu-metal about 0.16 mm thick, using the configuration depicted in Fig. 9. The only other significant problem was noise induced into the μPC readout system, which shares a crate with the FADCs used to read out the neutron signals. The noise was reduced by grounding all neutron signal cables with additional braids to the FADC crate.

3.8 Ge and NaI detector

The goals of a muonic X-ray detector in the MuSun experiment are twofold. First, prompt muonic X rays, i.e. in coincidence with the entrance counters, can provide information about 50% of the muons which do not stop in the TPC's fiducial volume. Secondly, delayed muonic X-rays can help determine the impurity concentration, mainly from oxygen (O) and nitrogen (N). In the MuCap experiment, the O and N impurity capture recoils, yielding signals of 300 - 500 keV, were well separated from all other signals in the TPC. In the MuSun experiment, many ^{3}He fusion pulses can also be found in this energy region (Fig. 18). Muonic X-rays are emitted with near 100 % probability when a muon transfers from μd to a carbon or oxygen atom. These X-rays, with energy from 100 to 170 keV, can be used to tag a capture recoil candidate in the TPC. After stringent TPC cuts to suppress fusion, X-ray tagging might provide sufficient sensitivity to identify capture recoils. With ppb level impurities, a total X-ray detection efficiency of about 1 % at 100 keV will yield more than 1000 tagged capture events over a whole run.

Using X-rays to identify materials in which the muons stop (Al, Fe, Si) requires the superb energy resolution of a high-purity germanium (HPGe) detector. However, with such a detector, it is too expensive to reach the required 1 % total detection efficiency to tag sufficient capture-recoil events (from N and O gas impurities) in the TPC. If the signal to background ratio is satisfactory, a NaI detector would be a good alternative. During the second half of the 2011 run, both a HPGe and a NaI detector were installed and tested.

A planar HPGe detector[2] with a 1.5 mm thick crystal was positioned horizontally, facing the center of the TPC at a distance of 39 cm, resulting in a ∼0.1 % detector efficiency at 100 keV. A fast and slow integrated signal were sampled by custom-built FADCs. After optimizing the ground connections, an energy resolution of 1.5 keV FWHM at 122 keV was achieved. Roughly 30 hours of muon data at the optimal running conditions were collected, after which, for unknown reasons, the crystal heated up. A second HPGe[3] detector with a 44 mm thick coaxial crystal was successfully installed at the same position, and was operational during the systematic temperature scans at the end of the run (Sect. 4.3.2). The shorter snout of this detector resulted in a factor of two loss in solid angle. A NaI detector (3 x 3 inch crystal) was installed at the same distance from the TPC as the HPGe detector, resulting in a similar efficiency at 100 keV. Both the raw PMT signal and a shaped signal were sampled by the FADC. The energy resolution was 15 keV FWHM at 122 keV. The NaI detector collected data continuously during the last 10 days of the 2011 run, including the systematic studies.

4 Analysis Roadmap

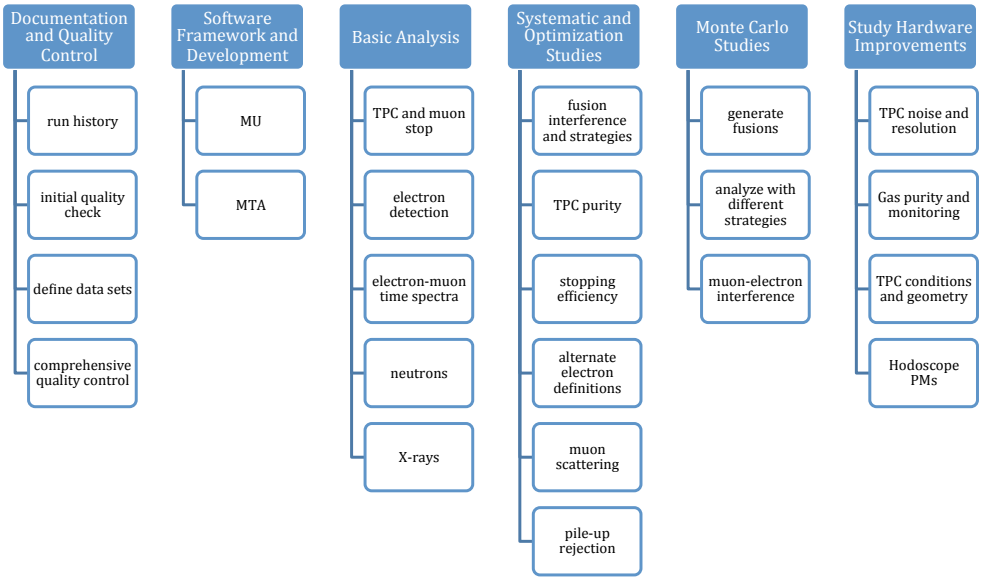

Figure 10: Outline of MuSun Analysis Plan, see text.

We are in the process of defining an analysis roadmap directed towards two main goals. First, we want to extract an initial MuSun physics result for Λ_d from the R2011 data. Secondly, we plan to evaluate, prepare and implement detector upgrades during this year, to optimize

[2]Model: Princeton Gamma-Tech MIGP 2013
[3]Model: Canberra GC2018

the MuSun apparatus for the final data taking in 2013/14. This plan is outlined in Fig. 10. "Documentation and Quality Control" refers to the classification and selection of high quality runs, which is well underway. The analysis framework has been significantly streamlined: by i) removing MuCap specific features, ii) designing structures to efficiently handle the complete record of digitized waveforms from the TPC and iii) making the software more accessible to a new user base in the MuSun collaboration. During the last year the number of code developers tripled. Three undergraduates and six graduate students as well as several postdocs and faculty members are collaborating on the analysis. The current status of the "Software Framework and Development" is described below. Initial steps have also been taken on "Basic Analysis" topics, with the main emphasis on recognizing muons in the TPC, but also on improving our understanding of electron detection and on developing auxiliary detection methods for systematic studies. Still, several detailed "Systematic and Optimization Studies" need to be developed and performed. The final MuCap results demonstrated that critical systematic issues could be addressed at the required level of precision. Thus, the following discussion will not be comprehensive, but focused on challenges which are specific to MuSun. Good progress was made on the development of realistic "Monte Carlo Studies", which will be essential for understanding and controlling the systematic errors. The category "Study Hardware Improvements" are studies to prepare and evaluate the hardware upgrades planned for 2012. In the following we cover some selected topics of the analysis roadmap together with first findings from R2011.

4.1 Analysis Framework

The primary computational platform for the MuSun analysis is the TACC Lonestar computing cluster, located in Austin, Texas, USA. On Lonestar, MuSun has limited dedicated project disk space, which reduced the staging efficiency for a large data set, but 500 TB are available in temporary scratch space. New analysis computers purchased by the collaboration proved invaluable for real-time offline analysis during the run. Other computer resources are being developed and tested, such as a local cluster connected to a 30 TB file storage array at the University of Washington. The recently-purchased computers form part of that cluster.

The MuSun data analysis software is a multi-stage, modular program designed for efficient use of computer time, reduction of data volume, and development by multiple analyzers. The first stage of the program ("MU"), written in C++ using MIDAS and ROOT libraries, collects raw data into physics objects such as electron or muon tracks, performs CPU intensive calculations like TPC pulse-finding, and stores the data in the ROOT tree format. The structure of this program is built on the modular MIDAS analysis framework such that individual analyzers can easily include personal specific calculations while having access to the developments of others. The second stage of the analysis ("MTA") is a flexible platform for quick passes over this tree output and consists of mostly specific studies, such as developing a robust TPC tracking algorithm.

The input to the first stage is the 1.5 GB data files recorded at PSI, containing approximately 1,500 MIDAS events, which are 140 ms periods of DAQ live time, collected over 3 minutes. The first stage program typically takes 30 minutes per file to run on the Lonestar computing cluster, where the largest single consumption of CPU time is the chi-squared minimization fitting of TPC pulses. The TPC pulse fitter was originally performed with ROOT's Minuit, but a customized fitter developed in the last year has yielded an order of magnitude increase in speed. The output of this first stage is a 1.6 GB ROOT tree file containing 4M "muon events." An event, defined by a muon signal in the beamline detectors coincident with a kicker transition, contains all the detector data within 35 μs of the muon entrance.

4.2 Basic Analyses

4.2.1 TPC and Muon Stop

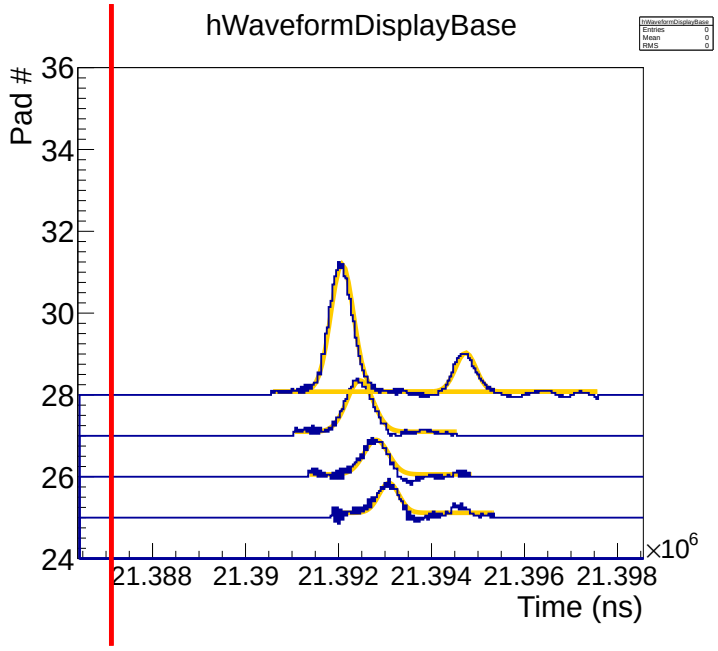

Figure 11: TPC signals of a muon track followed by a ^3He fusion product. The orange lines are the fit functions overlaid on the raw signal. The red line is the muon entrance time.

Pulse fitting

Most of the waveforms generated in the TPC are reasonably well-described by a gaussian profile, with the notable exception of the protons from fusion events. However, a better representation is obtained using a template method pioneered by the muon g-2 experiment at BNL. The pulse template is formed by fitting a large number of pulses to a gaussian waveform. Those waveforms are scaled to unit amplitude and width, then aligned to a common pulse center using a very fine time grid. We use the template thus-formed (which is **not** gaussian) to fit pulses from other runs, adjusting the peak time, and scaling the width and amplitude as needed. In principle, we should fit for the pedestal as well. However, since the pedestal on a given TPC channel is very stable over many runs, we have often fixed the pedestal in our fits. It is not yet clear whether this results in a significant systematic error in the amplitude measurement.

Although their noise properties vary, a single pulse template can be used to describe the signals from all pads (see Fig. 12, left). The chi-squared distribution for the gaussian and template fits are shown on the right - the template fit is noticeably better. The muon stop signal varies in amplitude depending on the position of the stop relative to the pad boundaries and in width depending on the pitch angle. The pulse shape does not vary significantly with amplitude or drift time.

The pulse-fitting algorithm works well on isolated pulses formed by stopping muons. The high-frequency noise (Fig. 12 and Sect. 3.1) can be filtered out of an otherwise presentable pulse without serious degradation of the algorithm's performance. The algorithm has not been optimized for the separation of overlapping pulses. Nor does it handle well the highly asymmetric pulses produced by protons. The ^{3}He and triton signals, however, are well de-

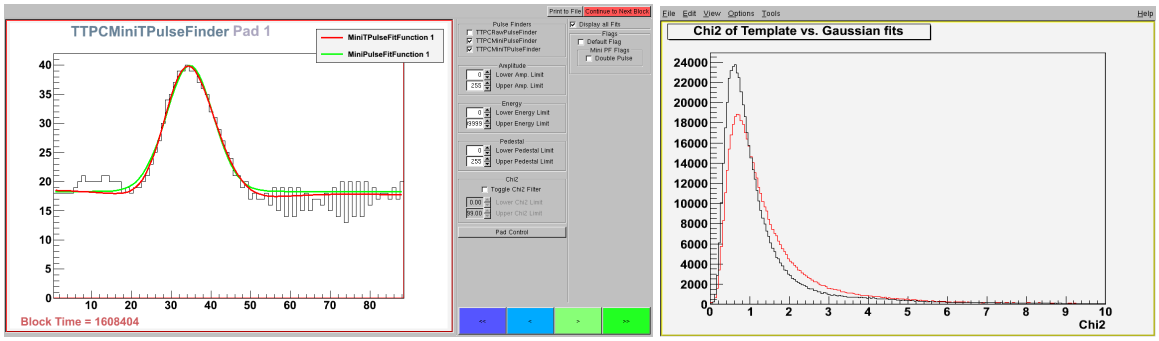

Figure 12: Left: Typical pulse with gaussian(green) and template(red) fits. Right: Distributions of chi-squared for gaussian (red) and template (black) fits overlaid.

scribed by the stopping-muon template. Data from any waveform which does not fit well to the template, in the initial production pass, is preserved for further consideration in a second pass.

Only a handful of particle types are observed in the TPC. There are muons, which stop or not, plus the charged particles produced in fusions and captures: protons, tritons, ^{3}He. Of the latter group, only the proton travels a significant distance in the chamber gas. If the muon stops over the center of a pad, the pulses produced by it and possible fusion products are relatively easy to understand. ^{3}He fusions appear as large symmetric pulses on the stopping pad. Triton pulses from p-t fusions are also symmetric and well-localized. Proton signals are far more varied in appearance. If the proton recoils vertically, its ionization energy will be spread in time. The resulting pulse will be distinctly asymmetric with the Bragg peak early(late) for downward (upward) going protons. A sample Monte Carlo event is shown in Fig. 13. If the proton travels horizontally, its energy may be shared over two or even three pads but the pulses will be far narrower and quite symmetric. Since most protons travel in neither the horizontal or the vertical plane, most proton signals will combine features of both. Event topologies are also complicated by particles who travel along, or stop near to pad boundaries.

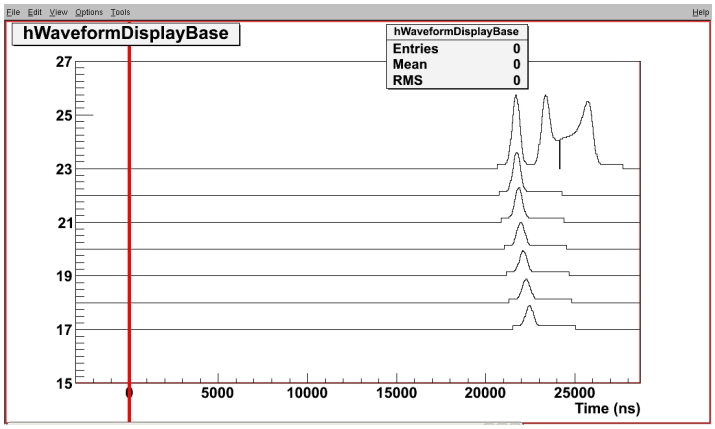

Figure 13: Monte Carlo waveforms delayed proton(up) plus triton(down) event

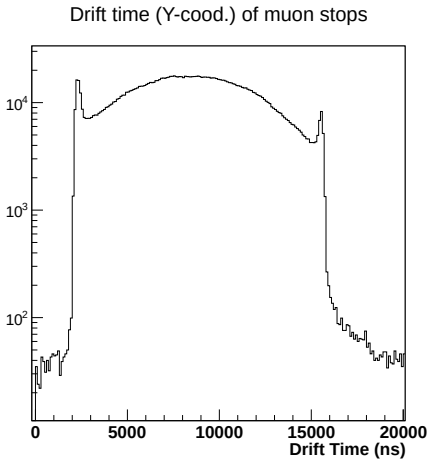

Figure 14: Vertical stopping distribution of muons, in the direction of the TPC drift (Y). The spikes on either end are all the muon tracks that hit the cathode or anode.

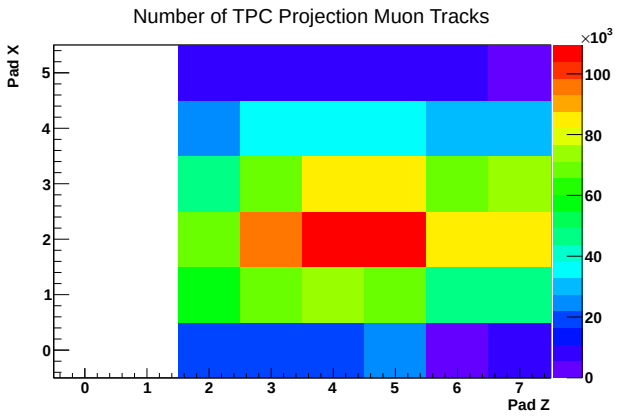

Figure 15: Stopping distribution of muons in the beam direction (Z) and transverse (X). The first two pads show no muon stops due to the stopping definition employed, i.e. requiring a signal on at least 3 pads in a row.

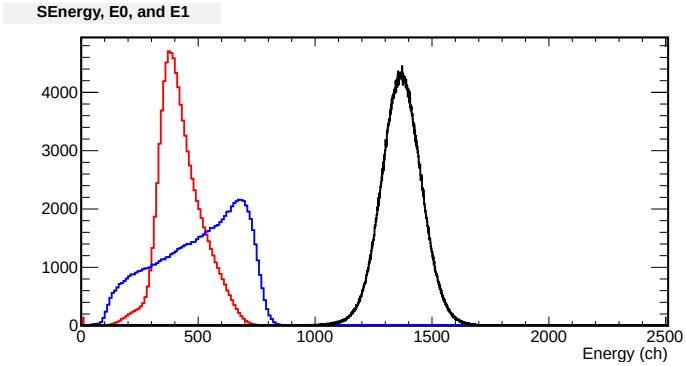

Figure 16: Energy deposition in the last pad (E0, blue), second-to-last pad (E1, red), and the well-peaked S-Energy, which is 2×E1 + E0.

Muon Tracking

The fitted pulses are used to find tracks in the TPC, independent of other detector information. Pulses within a window of 2 anode pads in the beam direction, 1 pad transverse to the beam, and 10 mm vertically are grouped into clusters. If there are at least 3 pads in a row in the beam direction, the cluster is considered a muon track. The only energy cuts are those imposed by the pulse fitter and the digitizer threshold. Because a muon stopping on an edge pad and a muon traveling beyond the active region of the TPC look similar, stops outside a smaller fiducial volume are vetoed. Energy cuts are avoided in the stop definition because this couples the acceptance of muons to the presence or absence of pile-up fusion events, which are time-dependent.

Once the stopping location of the muon is known, properties of the tracks can be studied. The distribution of stops is peaked slightly to the back of the chamber (Fig. 15), to allow each muon track to have a sizeable tail. In the vertical (y) direction, the coordinate is given by the drift time in the TPC (Fig. 14), where the drift velocity is 5 mm/μs. The energy deposited in the stopping pad depends on how deep into the pad the muon stopped. The last

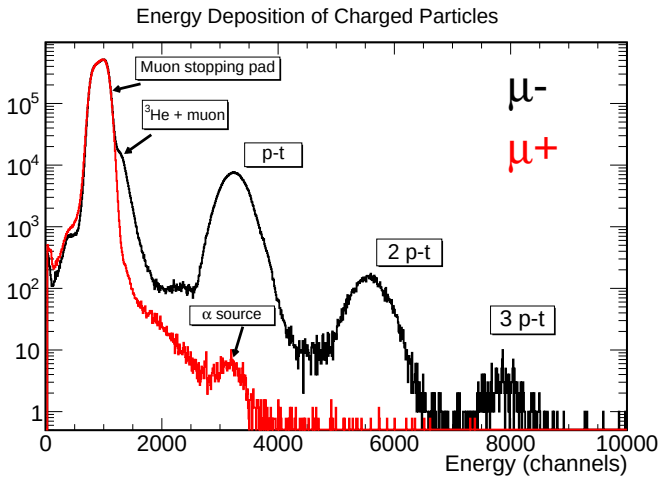

Figure 17: Charged particles in the TPC. The energy deposited on the stopping pad and all neighboring pads is summed for each event, showing the fusion products in pile-up with the muon stop.

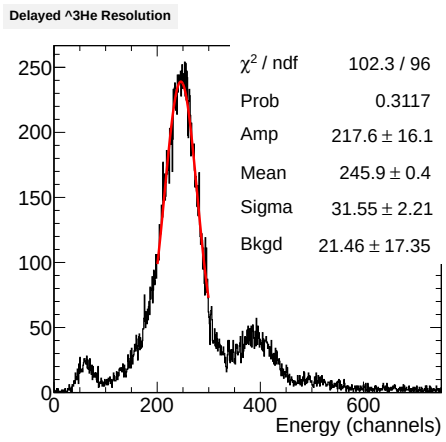

Figure 18: The ^3He and $^3He\mu$ energy peaks for delayed fusion events in a single pad. The monochromatic peak can be used to calibrate the TPC, pad-by-pad. Because the singly-charged μ^3He suffers from less recombination, the peaks are separated.

pad could collect the full Bragg peak or barely enough to trigger the hardware or software thresholds. However, the combination of the stopping pad energy plus twice the previous pad energy, referred to as the "S-Energy," is found empirically to be a well-peaked (Fig. 16), and is useful to represent the muon stop energy with a single value.

The energies of charged $dd\mu$ fusion products are easily measured in pileup with the muon track, as in Fig. 17, but disentangling the particles' signals is difficult. One technique is to look for delayed fusion events, where the track ionization has drifted away from the muon, separating the pulses in the TPC. A library of fusion waveforms, constructed from these delayed fusion events, would be a valuable tool to systematically study the effect of adding a fusion signal on top of an otherwise clean muon stop. The ^3He signals are usually smaller than the muon stopping signals, so delayed events are required to get clean pulse separation and identification. The $dd\mu \rightarrow {}^3He(0.82MeV) + n(2.54MeV)$ reaction produces a monoenergetic ^3He, providing an isotropic calibration source, as well as a measurement of the energy resolution of the chamber (Fig. 18).

Protons produced in the reaction $dd\mu \rightarrow p(3.02MeV) + t(1.01MeV)$ are not localized like the ^3He and t, having enough energy to travel 16 mm (one pad length) at the nominal gas conditions.

4.2.2 Electron time spectra

Fig. 19 shows a lifetime spectrum and fit for a data set of 5.7×10^7 μ^- decays and 3.5×10^7 μ^+ decays. For the muon, we required a pileup-protected entrance and subsequent stop in the fiducial volume. For the associated decay electron, we required a reconstructed electron track in the ePC's and a four-fold coincidence in the electron scintillator hodoscope. The lifetime histogram is then filled with the time difference between the electron scintillator signal and the entrance scintillator. These initial fits of a limited set reveal no major systematic issues for the 2011 data and our current analysis procedures. The full R2011 data set will be analyzed once robust and well understood event selection criteria are developed.

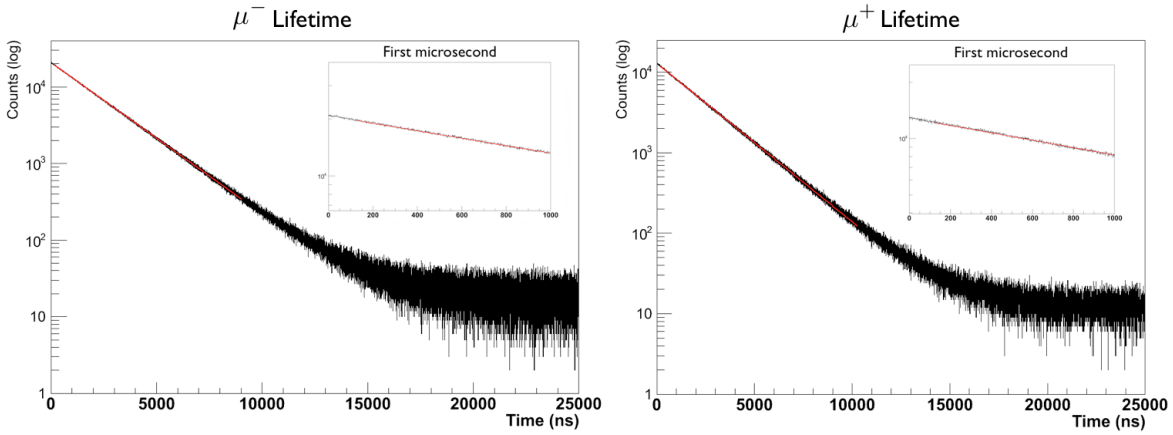

Figure 19: Fit to the electron decay spectrum for μ^- (left) and μ^+ (right). Both time spectra were fitted from 200 ns to 10 μs, yielding a χ^2/ν of 1.16 and 1.09, respectively.

4.2.3 Neutrons and X-ray detection

Neutrons

Neutron analysis goals from this run include: standardizing the calibration procedure and optimizing pulse shape discrimination, studies of the fusion neutrons to determine our sensitivity to the $dd\mu$ formation rates (λ_q and λ_d) and hyperfine transition rate (λ_{qd}), studies of the low-energy neutrons from the μd capture reaction and from possible high-Z sources, maximization of signal rates, signal-to-background and resolution.

Calibration data was taken with a Co-60 and Cs-137 source on a regular basis and under different experimental conditions, e.g. with the μSR magnet on and off. The Compton edges[4], used for the energy calibration, were modeled by a convolution of the Klein-Nishina differential scattering cross-section for Compton scattering and a Gaussian (see Fig. 20). The table below shows the gains for all detectors using this method.

Counter	Gain (ch/keV)	Counter	Gain (ch/keV)
NU3	7.32	NU11	7.75
ND3	6.41	ND11	8.58
NU6	6.7	NU14	4.22
ND6	6.38	ND14	5.25

Table 3: The table shows the gains of all neutron detectors, 'D' stand for downstream, 'U' for upstream, and the number stands for the position in ϕ.

Neutron and γ ray pulses can be distinguished on the basis of their pulse shapes. The total pulse integral was defined as the area under a region of the pulse that extends from -17.6 ns to +117.6 ns relative to the constant fraction time t_0 of the pulse (half peak value). Slow integrals are defined as the area of the tail region of a pulse with various windows, which are currently being optimized. As an example, Fig. 21 shows the slow integral, defined as the integral from t_0 + 29.4 ns to t_0 + 117.6 ns, versus the total integral. Slices of these plots are fitted to a sum of two Gaussian functions. The distance between the neutron and the γ peaks divided by the sum of their FWHM defines the figure of merit M, a higher M value indicating a better performance. Currently M=1 is achieved at 200 keV.

[4] 0.98 MeV and 1.11 MeV for ^{60}Co and 0.48 MeV for ^{137}Cs

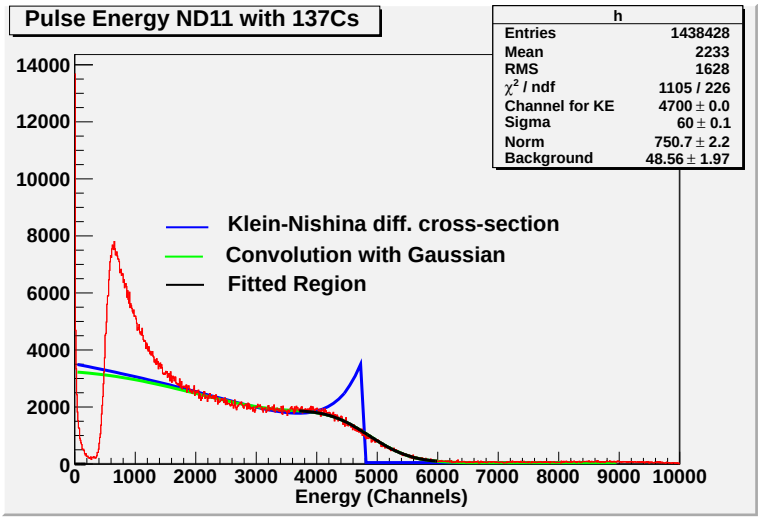

Figure 20: Convolution of Klein-Nishina and Gaussian for the 'ND11' neutron detector, using ^{137}Cs as a calibration source.

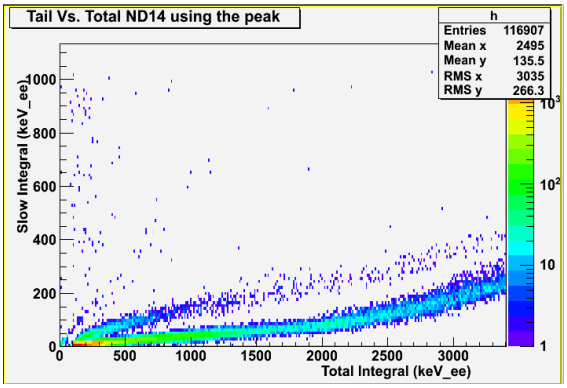

Figure 21: Slow integral, integrated from 5 to 20 time bins to the right of the 'peak half-amplitude' time, versus total integral. The higher band corresponds to neutrons, the lower to γ rays.

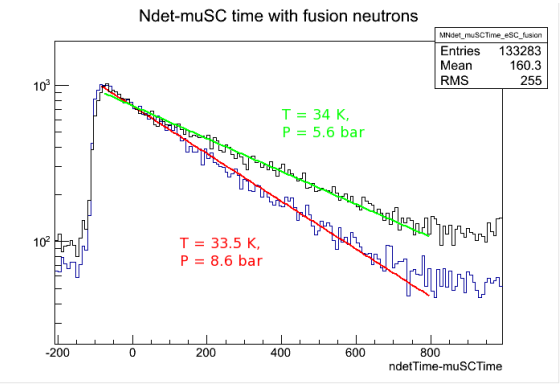

Figure 22: Fusion neutron time spectra for two different density conditions

A deuterium density scan was conducted by varying the temperature between the nominal value of 34 K up to 42 K, and the pressure between the nominal value of 5.6 bar up to 9.5 bar. The comparison of the neutron time spectra at different density conditions can help to determine the hyperfine transition rate λ_{qd} (Sect. 3.7). Fig. 22 shows the fusion neutron time spectra for two different density conditions.

X rays

In the first, "MU-level," analysis stage, X-ray hit objects are constructed from the sampled waveforms, combining the fast timing signal with the slow energy signal (two for the HPGe detector), storing the constant-fraction time and pulse amplitude. In addition, a pile-up and pulse-quality flag is set. In the second analysis stage the X-ray detector hits are combined with physical objects from the other detectors, such as a muon entrance or an electron track.

In between production runs, calibration data was taken with a ^{57}Co, ^{60}Co and ^{137}Cs source

on a regular basis. For the *optimal* dataset (see Sect. 3.8), the NaI detector had a dynamic range of 1.5 MeV, and 2.5 MeV and 750 keV for the low and high-gain channels of the HPGe detector, respectively. For beam-on data, the gain stability is monitored by the ever-present 511 keV $e^{\pm}$-annihilation line. A major background contribution comes from Michel electron related bremsstrahlung, which is largely removed by using the electron-detector sectors right in front of the X-ray detectors as a veto.

Fig. 23 shows the time distribution of the germanium detector hits relative to the muon entrance. Detector hits associated with a *good* muon stop, i.e. in the TPC fiducial volume, are described by a single exponential following the muon life time. The spectrum of detector hits associated with muons which do not stop in the fiducial volume show a prompt peak. Conversely, X-ray detectors can be used to test a muon stop definition. A time resolution of 33 ns FWHM is derived from the prompt peak at -200 ns (insert in Fig. 23). At later times, detector signals originate from decay electrons, capture neutrons and γ-rays. These delayed signals are indeed not muonic X-rays, as almost all discrete lines in the energy spectrum disappear after 100 ns (Fig. 24).

Fig. 25 shows the prompt germanium detector hits with an additional cut on Michel electrons, in this way separating X-rays from high-Z and low-Z muonic atoms, as high-Z nuclei are more likely to capture the muon. Most X-rays are produced by high-Z materials such as iron and silver (see Sect. 3.4 for TPC materials). Inclusive of a delayed electron cut, Fig. 25 reveals a small oxygen X-ray. The two detectors are currently being implemented in the MuSun GEANT4 code (Sect. 4.4) to calculate their absolute efficiencies and to further understand the number of observed X-rays. The data presented in these figures were produced from 180 runs from R2011, with a total of 4.8×10^8 pile-up protected muons.

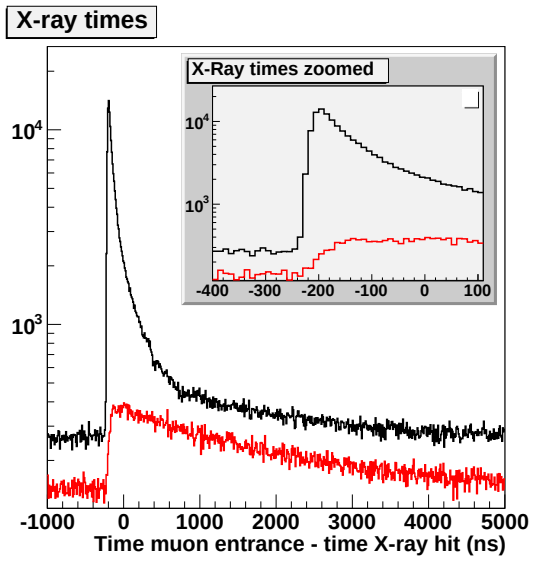

Figure 23: Time distribution of the X-Ray detector hits. The hits associated with a muon stop in the fiducial volume are shown in red and follow the muon life time, the others in black.

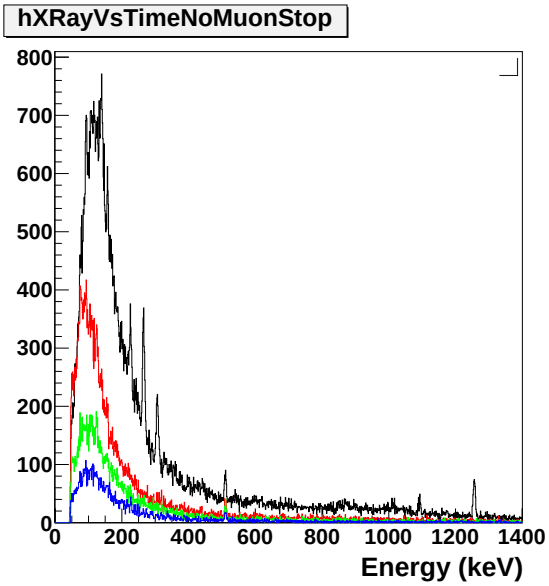

Figure 24: The germanium detector's low-gain energy spectrum with a 90 ns wide time window around the muon entrance (black), and a delayed one by 100 ns (red), 200 ns (green) and 400 ns (blue), respectively.

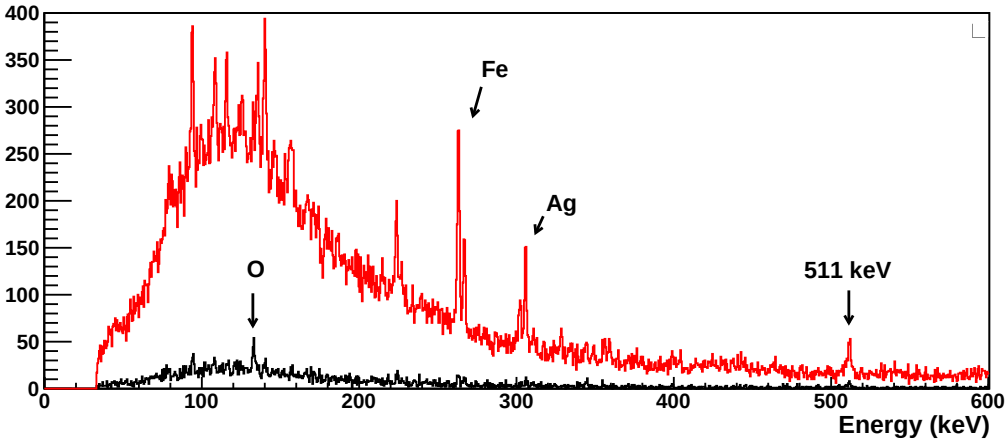

Figure 25: Prompt germanium energy spectrum, with (black) or without (red) a delayed electron, separating high from low Z elements. The 133.5 keV 2p-1s K-line from O, the 269.4 keV and 265.7 keV 3d-2p L-doublet from Fe, and the 308.4 keV and 304.8 keV 4f-3d K-doublet from Ag are identified. The main 1255 keV K-line from Fe shows up in the low-gain spectrum (Fig. 24). X-ray energies from ref. [9] and [10].

4.3 Systematic and Optimization Studies

4.3.1 Fusion interference

Muon-catalyzed fusion is a new feature in the MuSun experiment, compared to MuCap. Fusion events play a dual role. On the positive side, they serve as a powerful monitor to prove that the muon kinetics is quantitatively understood. The ^{3}He recoil also provides a local, well-defined energy deposition, useful for resolution studies. On the negative side, interference between fusion and muon-stop identification must be scrupulously avoided. Since the fusion signal indicates that the muon has lived at least up to the moment of fusion, the time distribution of electrons with a fusion requirement is different from the pure exponential of decay electrons after a muon stop. Let us define the fusion distributions as $p_f(t_f) = e^{-\lambda t} f(t_f)$, where $f(t_f)$ follows from the solutions of the kinetic equations [7], and the electron distributions as $p_e(t_e) \equiv e(t_e) = \lambda e^{-\lambda t}$. The probability to have a fusion at time t_f and electron at time t_e is then $p_f(t_f)p_e(t_e - t_f) = f(t_f)e(t_e)$. Integrating the last equation, the observed electron distributions can be expressed as

$$P_e(t_e) \propto e^{-\lambda t_e} \left(1 - \int_0^{t_e} f(t_f)\eta(t_f)dt_f\right) \tag{2}$$

where $\eta(t_f)$ is the change of the muon-stop acceptance if a fusion happens at time t_f. If the muon stop is unaffected by fusion, $\eta(t_f) = 0$, and the correct electron time distribution can be recovered. The dominant causes for fusion/muon-stop interference are fiducial and quality cuts in the selection of a muon stop. The 0.82 MeV ^{3}He (0.80 MeV μ^3He) fusion products are less of a problem, as they are short-ranged, traveling 0.18 mm (0.6 mm) compared to the 16x16 mm^2 anode pads. More dangerous is the proton from p(3.01 MeV) + t(1.01 MeV) fusion, with a range of 16 mm at our target conditions. The triton is stopped within 1 mm. The effect of this correction in Eq. 2 has been studied analytically and with simulations. Typically knowledge of $\eta(t_f)$ to a few 10^{-3} is required in order to affect the extracted capture rate by less than 4 Hz.

Different strategies to design a muon-stop finder insensitive to fusion are being explored. One follows the idea of a *muon-stop cut*, where the muon is constrained to a rectangular

fiducial volume inside the TPC. Such a selection eliminates background from muon stops in the wall, but results have to be corrected for "proton leakage": events where the muon actually stopped inside the fiducial volume, but is misreconstructed to be outside because of the pile-up from a proton track. Another approach implements an *upstream cut*, which uses only pads at least two rows upstream from the stop pad, which are out of reach for the proton. As a variant, one could just use the TPC entrance pads to define the muon stop, though the background will be larger than in the other methods.

The first step towards this goal is the careful study of fusion products and their properties. The positive muon stop should produce a similar signals in the TPC, but without fusion products. With negative muons, well-separated delayed fusion waveforms can be extracted as described in section 4.2. They will be compiled into a library that can be used to artificially impose a fusion signal on top of a clean positive-muon stop. By varying the time delay between the signals, one can reproduce all possible natural overlaps. This allows a data driven approach towards determining $\eta(t_f)$. At the same time Monte Carlo simulations are essential to understand the interference topologies and guide the development of the event reconstruction (c.f. section 4.4). As a next step, the production of a medium-statistics Monte Carlo data set is being prepared; the $p+t$ production will be enhanced from 3%, as is typical for our target conditions, to 100%. This data will serve as a benchmark to test the robustness of various muon stop finders against fusion interference.

4.3.2 TPC purity

For MuSun, D_2 gas at a purity level of parts-per-billion (ppb) has to be produced and maintained during running periods of several months. This critical and challenging task must be achieved by the continuous gas purification system CHUPS, and the purity has to be verified. The requirements are derived from the parameters in Table 4 (from [7]).

Element	λ_{dZ}	$\Lambda_{dZ}(s^{-1})$	$\Delta\lambda(s^{-1})$	Y	$\Delta\lambda/Y$
N	$1.45\ 10^{11}$	$9.3\ \frac{c_Z}{ppb}$	$2.0\ \frac{c_Z}{ppb}$	$2.7\ 10^{-6}\ \frac{c_Z}{ppb}$	$0.76\ 10^{-6}$
O	$0.63\ 10^{11}$	$4.0\ \frac{c_Z}{ppb}$	$1.2\ \frac{c_Z}{ppb}$	$1.6\ 10^{-6}\ \frac{c_Z}{ppb}$	$0.71\ 10^{-6}$

Table 4: λ_{dZ}: transfer normalized to LH_2 density, Λ_{dZ}: effective transfer rate at MuSun condition for c_Z in ppb, $\Delta\lambda$: resulting change in observed lifetime, Y: capture yield on impurity.

For the main production part of R2011, the TPC was operated at T=34 K, P=5.6 bar, corresponding to a density of ϕ=0.064 relative to LH_2 density. Fig. 26 indicates that most common impurities are expected to be cryopumped to the walls, except for N_2 and O_2.

Gas chromatography

Samples were delivered from a sampling port that was situated at the closest possible point to the cryo-TPC, through a 8 m capillary stainless steel line that was brought out of the beam area directly to the chromatograph. Chemical impurities were first accumulated in a column filled with adsorbent and cooled to liquid nitrogen temperatures. Then they were pushed out from the column into the chromatograph by heating. The chromatograph lines and the interior of the apparatus were cleaned by continuous flushing of the tubes and vessels by purified helium. Several samples were taken from the system during the run. The sensitivity limit obtained using the method to calculate the oxygen and nitrogen traces strongly depended on the volume of the sample. The best results corresponded to a 50-L probe with 5 L spent for the flushing of the system. This probe gave $O_2 < 0.4$ ppb, $N_2 < 1$ ppb. Actually, neither

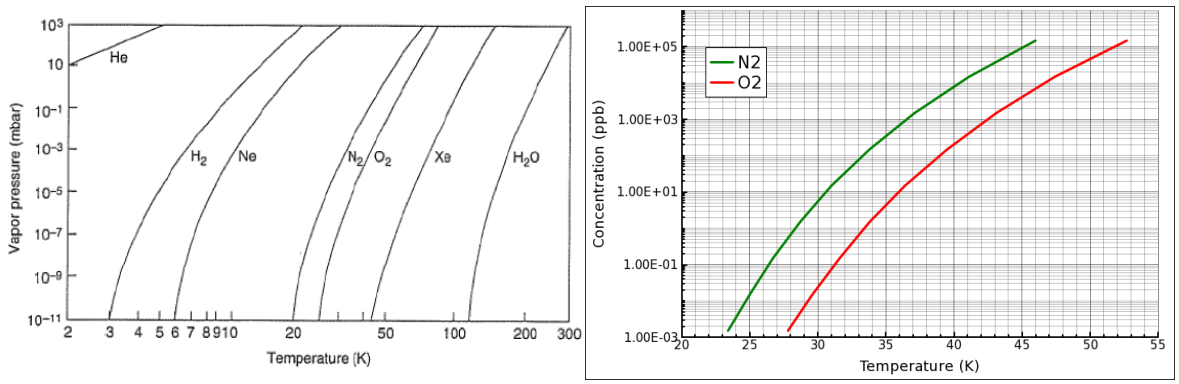

Figure 26: Left: Vapor pressure curves; Right: calculated equilibrium concentrations for N_2 and O_2 relative to MuSun gas density as function of temperature.

of the components was visible, being below the sensitivity threshold. To provide the isotopic analysis, the configuration of the chromatograph was modified. The separation column was changed to one packed with a more suitable zeolyte, neon was used as a carrier gas, and a direct sampling procedure without preliminary enrichment was applied. This analysis found 20±20 ppm of HD at the beginning of R2011 (after the isotopic separation procedure), and 180±20 ppm at the end.

Signal losses during drift in TPC

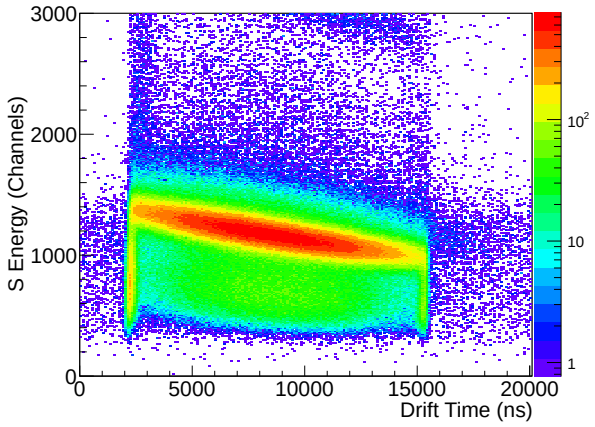

Figure 27: The S energy vs. drift time for run 54601, when the TPC was at 50 K (Fig. 28).

The signal as function of drift time was measured using the S-energy. The data in fig. 27 shows that muon stops near the TPC cathode, whose ionization must drift through the entire TPC volume to the anode plane, produce smaller signals than muon stops near the anodes. This effect is parameterized as the signal amplitude loss (in ADC channels) per 5mm drift distance, which is the vertical axis in Fig. 28 (left). Several effects could be responsible for such losses. However, we also observed a change of the slope, when changing the TPC conditions. In the chronological plot (right), the TPC is initially closed to CHUPS flow, enforcing a constant gas density, and then heated in steps to 50 K. The signal loss at 50 K does not change until run 54730, where the TPC is opened to CHUPS flow, at which point the signal loss exponentially damps towards a value of 8 ch/5 mm with a decay constant

of 10 hours. In Fig.28 (left), the black curve indicates the heating of the closed TPC from 34 K to 50 K, showing a steep rise followed by the onset of saturation. The blue curve is the period with CHUPS flow at 50 K and the red points show the decreased signal loss at fixed temperatures on the way back to the nominal 34 K. Unfortunately, this was near the end of the beam period, so the trend could not be followed. But on returning the gas to 34 K in steps, the signal loss was less than it had been before the CHUPS flushing.

As oxygen is a well-known electronegative contaminant, traces of oxygen could explain this temperature dependence. If there was frozen oxygen on the walls of the TPC, the partial pressure would show such a dependence followed by saturation when all of the oxygen is evaporated. Because the partial pressure is small (∼2 ppb) at normal running conditions, the continuous flux of the CHUPS system would never pump out any appreciable volume of oxygen, which is why there is no variation of the signal loss with time. However, while the temperature is elevated, a significant quantity of the oxygen is gaseous, allowing CHUPS to flush it from the system, which could explain the improvement upon returning to nominal conditions.

The saturated oxygen level of 2 ppb is extremely low compared to usual drift chamber conditions, but we are not aware of experience with deuterium/oxygen mixtures at cryogenic conditions. Moreover, the chromatography results do not confirm such oxygen contamination. As the gas purity is a main concern, we plan to investigate these effects carefully. This includes a complete analysis of the data and the verification of the chromatographic sensitivity. We are exploring the possibility to detect impurities in situ with combined TPC and X-ray detection. Clearly, the cleaning procedure before the run must be improved and the CHUPS flow increased, as the cryo-pumping effect might be insufficient.

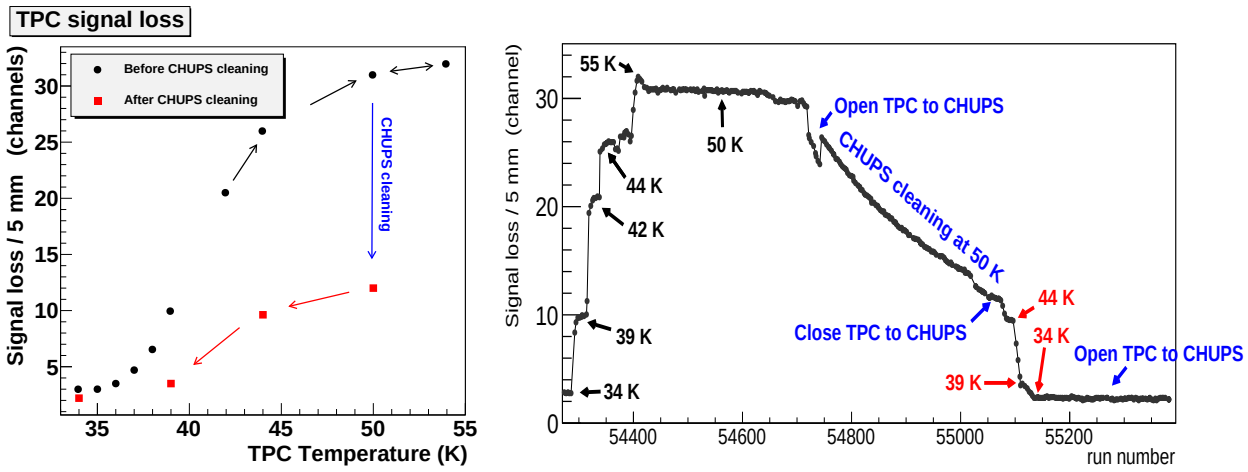

Figure 28: The signal loss effect versus temperature (left) and chronologically (right).

4.4 Monte Carlo

The MuSun GEANT4 simulation was largely in place at the beginning of 2010. Much of the work that had gone into its development in previous years was focused on two areas. First, precise geometry upgrades were implemented, with a special focus on the accuracy of volumes near the fiducial region. This allowed the simulation to be used for many time-sensitive studies throughout the last year, many of them on-site at PSI. For example, during the Fall 2010 run, there were concerns that the percentage of muons that stop in the TPC depended on the beam entrance point on the front of the beryllium window. Since the beam could not be steered onto the desired entrance point, a time-consuming displacement of the TPC was

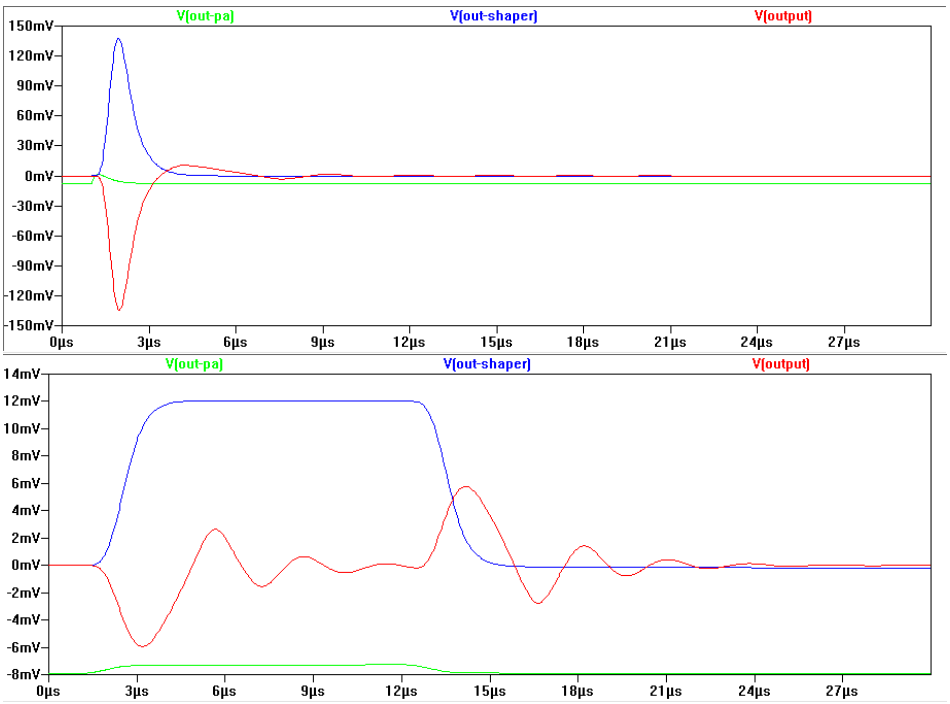

Figure 29: LTSpice pulse shapes for input corresponding to 4 fC of ionization charge, deposited over 0.01 μs (top) and 10 μs (bottom). The green, blue, and red traces show the output of the preamplifier, shaping amplifier, and baseline restorer. Note that a vertical proton from a proton-triton fusion yields a 3.2 μs long signal.

considered. However, the simulation demonstrated that effects of shifts in the beam position would be minimal. The simulation has also helped answer questions about the TPC pad plane material. Muons which are Coulomb scattered downward could fake a valid muon stop and then capture on the pad plane. The proposed solution was to place a layer of gold over the conducting pad segments. The simulation showed that the frequency of these faked stops was problematic but that the deposition of a 20 micron gold layer on the pads would suffice to mitigate the effect on the lifetime.

Secondly, additional work has been put into coding new classes of decays and fusion channels. Simulation users can not only choose from among these various processes, but also specify the time and momentum of the daughter particles from each reaction. This step has allowed us to perform some new analyses, and approach older studies from different angles. One such example is that of electron interference with muon tracks. Alerted to this issue by the MuCap experiment, the collaboration found that electrons could induce shifts on their parent muon's signals. Although both TPCs are optimized for muon detection, ionization from some downward-going decay electrons can interfere with the muon signal. With the new simulation tools, the kinematics of the decay positron can be specified. The effect of these very small signals is now being studied. Another area that has benefited from these advancements is the fusion output. The pulse signature of the ^{3}He fusion channel is relatively tame, as the helium nucleus has a very short range, at nearly 1 mm. The proton + tritium fusion is much more daunting, as the proton travels approximately one pad length with three times the kinetic energy of the helium. The pulse shapes generated by the proton depend primarily on its recoil direction, and numerous overall event topologies depending on on the time and location of the fusion event.

With the updated simulation tools and Regis University's response framework for convert-

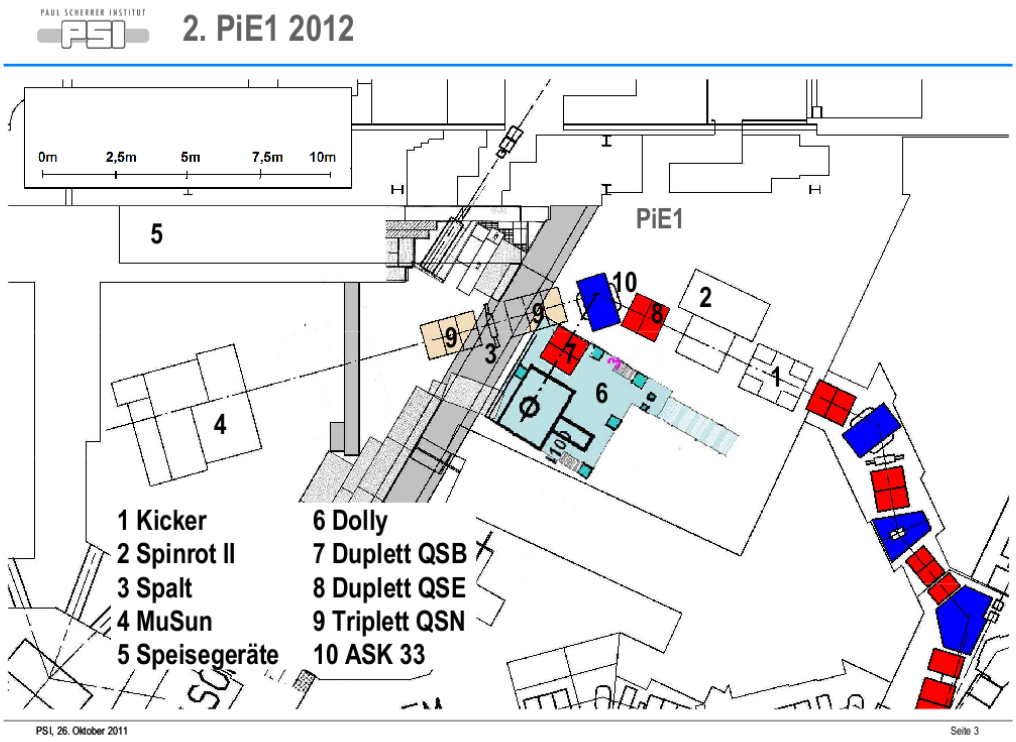

Figure 30: plan of the new expanded $\pi E1$ area making use of the former NE-A area.

ing Geant4 output into our collaboration's standardized MIDAS format, we have generated a myriad of fusion signatures. An analysis of this data has greatly improved our intuition regarding fusion-related tracks and their constituent pad signals, and will guide us in our track reconstruction strategy. Work is in progress to build a detailed model of the analog frontend electronics to make the Monte Carlo response program more realistic. An LTSpice simulation has been used to track the signal through the preamplifiers, shaping amplifiers, and baseline restorers for signals of varying durations and amplitudes. It reproduces the experimental pulse shape for short durations, and it demonstrates the effect of the baseline restorer on long pulses, such as those that would arise from vertically-oriented electron tracks. These pulse shapes are shown in Figure 29. These pulse shapes are now being parameterized for inclusion in the Monte Carlo response program.

5 Plans and Beam Time Request 2012

5.1 Development of expanded πE3 area

The planning of the expanded $\pi E1$ area has been greatly advanced by the PSI secondary beam group, as shown in Fig. 30. The basic idea of this project is to create space for a new low-energy muon beamline for particle physics experiments. It will replace the former $\pi E3$ beamline, which is now used exclusively for the high-field μSR facility. The MuSun experiment will be set up and operated in an expanded area that can be closed off from the present $\pi E1$ area so that other experiments can use the beam during MuSun setup. The Dolly μSR facility also profits from the new layout with a permanent operational space in the back left corner of $\pi E1$, so that its removal is no longer needed when other experiments are in the beam.

The present status is that the former NE-A area has been opened and emptied of all of the equipment previously there. The next step will be to replace the wall between the $\pi E1$ and NE-A areas by a bridge connecting them while maintaining access to the Aare side of the experimental hall. Further work will include creation of infrastructure for the expanded area (magnet power supplies, water, electricity, etc.) and preparation of all elements of the new beamline. The expanded $\pi E1$ area is expected to be ready by fall 2012, although the two new quad triplets in the MuSun beam section will not arrive before 2013 and therefore need temporary replacement by doublets.

5.2 Collaboration Plans and Tasks

5.2.1 Tasks and upgrades before the run

The development of the new πE1 beamline shifts the next MuSun production run into 2013. The collaboration intends to use the intervening time to make progress towards three main goals:

- Decisively move forward with the R2011 analysis, to achieve a first data reconstruction pass and address all systematic issues outlined in the previous section.
- Support the development of the new beamline, install the detector, electronics and experimental infrastructure at the new location, and eventually commission the beam.
- Upgrade and repair components of the apparatus based on the experience gained from the analysis to optimize the experimental systematics for final production in 2013-14.

As we have addressed the first two points already, we elaborate on the third point below.

TPC Noise and Resolution

The TPC energy resolution is critical in many respects. It determines our capability to define muon stop locations based on smaller upstream pad signals, to disentangle complex fusion topologies, and to monitor impurities in competition with fusion signals. We have improved the resolution by a very significant factor during 2011, but we believe that we have not yet reached its limit. Currently the preamplifiers are located outside of the vacuum containment, connected to the cold TPC by custom long transmission cables. This is the operationally safest solution, but it deteriorates the noise performance. For this reason a second TPC has been built by PNPI and will be equipped with custom built cryo-preamplifiers, which are located close to the cold TPC feedthrough inside the insulation vacuum. This is a very promising development project, but it will need to be tested extensively to assure reliable operation. The tests will be performed at the University of Washington and will not interfere with the existing TPC setup.

Gas Purity

An extended presence of the PNPI group at PSI is planned for fall 2012. They will repair the aging CHUPS purification system so that the performance parameters observed in MuCap can be regained–in particular, increasing the circulation flow rate. The TPC will be reassembled and cleaned, the cooling capacity improved, and tests of the new electronics and pad plane will be performed jointly with US collaborators. We will determine the feasibility of inserting a getter into the circulation system, which could dramatically increase the sensitivity of gas purity measurements compared to the present method of sampling of limited gas volumes from the circuit. This new method would need careful calibration. The R2011 data will allow us to

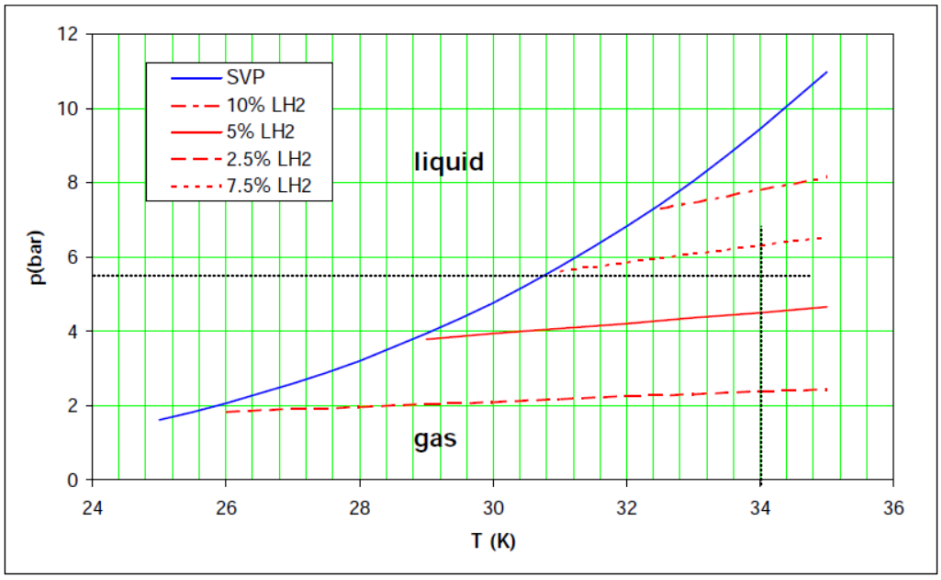

Figure 31: P-T diagram of cryogenic D_2.

estimate whether in-situ monitoring via capture reactions on impurities with a combination of TPC and X-ray detection an be achieved with sufficient sensitivity. Eventually, a pure protium run might be the most direct way to understand the subtle drift loss effect. In MuCap, we demonstrated that capture recoils can be clearly monitored to better than 1 ppb contamination level, if the TPC environment is free from muon-catalyzed background. As protium contamination of deuterium is a concern, we still have to work out a procedure for a pure protium run that would not impact later deuterium running.

TPC conditions and geometry

Several aspects of the TPC configuration should be optimized based on the R2011 analysis. As mentioned already in the experimental proposal [7], different pad geometry, granularity, and overall length should all be considered. Changes in the granularity are coupled to the cryo-preamp project, because at the moment the noise performance is dominated by cable capacitance, so that an increase in the number of cables would deteriorate the signal-to-noise. Covering all surfaces visible to the muon with high-Z material would be advantageous, in order to reduce effects from rare wall stops. While the top cathode has been silver-coated already, the gold plating on the anode pad plane is still too thin. We are developing the technology to improve this. Finally, the choice of gas conditions can have a major impact. Figure 31 shows the relevant P-T diagram for cryogenic deuterium, where the operational point of R2011 is indicated by the cross. If gas purity is a major concern, than decreasing the temperature to 30 K would dramatically reduce the saturation concentration of O_2 and N_2; this is illustrated in Fig. 26. Of course, it would very valuable to demonstrate the expected vapor pressure behavior by operating the TPC with pure protium, which allows a verification at the sub-ppb level. On the other hand, higher temperatures would allow for higher gas density, which implies better muon stop efficiency, better stop localization, and earlier quenching of the undesired μd quartet state. This optimization depends on ongoing analyses and further beam tests in 2012.

Electron detector

The large wire chamber ePC2 has been dismounted, and its broken wire will be replaced by the PSI detector group. Then the combined chamber system will need to be inserted, instrumented and commissioned again. The 64 aging photomultipliers of the scintillator hodoscope behaved unreliably during R2011; several tubes were unstable, and many showed a large number of afterpulses. We are considering replacing them with better ones. As we have a sufficient number of good, fast 2-inch photomultipliers from the muon g-2 experiment, the main issue will be to design a mechanical mounting compatible with the current detector structure.

5.2.2 Run Plan

The new πE1 area with extension toward the former NE-A area will be available starting in the fall (September-December 2012). The commissioning work will begin in the second half of September. The MuSun collaboration is committed to actively participate in this work with people, beam instrumentation and data acquisition.

In addition, we need access to the new NE-A part of πE1 for mounting and setting up the MuSun apparatus, in advance of our beam time. Thus, we request that during beam commissioning the MuSun detector is separated from the beam tests by a wall, so that we can systematically install the experiment in the new location without interrupting the beam activities.

After the commissioning we request beam time for a MuSun engineering run with the following goals.

- Commissioning the beam at the experiment. The initially commissioned beam including of the full transfer beamline, the fast MuLan kicker, and the ExB separator will be directed to the experiment. The TPC will be used to establish beam quality and rates at the measuring position in the new annex.
- The MuSun detector will be operated in the new experimental location. The various upgrades of the detector system and the cryo- and purification infrastructure will be tested.
- A measurement program will be directed towards the demanding purity issue. This will include temperature cycling with improved cleaning and monitoring systems.

5.3 Beam Time Request

For this program, we need and request a full 4 week period of πE1 beamtime, from Oct. 11 to Nov. 5, 2012. We also request access to the new NE-A part of πE1 for mounting and setting up the MuSun apparatus, starting one to two months ahead of the allocated beam period.

References

[1] MuSun Collaboration (http://muon.npl.washington.edu/exp/MuSun):
V.A. Andreev, E.J. Barnes, R.M. Carey, V.A. Ganzha, A. Gardestig, T. Gorringe, F.E. Gray, D.W. Hertzog, M. Hildebrandt, L. Ibanez, P. Kammel, B. Kiburg, S.A. Kizilgul, S. Knaack, P.A. Kravtsov, A.G. Krivshich, K. Kubodera, B. Lauss, M. Levchenko, X. Luo, K.R. Lynch, E.M. Maev, O.E. Maev, F. Mulhauser, M.H. Murray, F. Myhrer, A. Nadtochy, C. Petitjean, G.E. Petrov, J. Phillips, R. Prieels, N. Raha, G.N. Schapkin, N. Schroeder, G.G. Semenchuk, M.A. Soroka, V. Tishchenko, A.A. Vasilyev, A.A. Vorobyov, N. Voropaev, M.E. Vznuzdaev, F. Wauters, P. Winter.

[2] Kammel, P. and Kubodera, K. *Annu. Rev. Nucl. Part. Sci.* **60**, 32753 (2010).

[3] Marcucci, L. *arXiv:1112.0113 [nucl-th]* (2011).

[4] Bardin, G. et al. *Nucl. Phys.* **A453**, 591 (1986).

[5] Cargnelli, M. et al. In *Proceedings of the XXIII Yamada Conf. on Nuclear Weak Processes and Nuclear Structure, Osaka, Japan*, (1989).

[6] Chen, J.-W., Inoue, T., Ji, X.-d., and Li, Y.-C. *Phys. Rev.* **C72**, 061001 (2005).

[7] Musun Collaboration, Muon Capture on the Deuteron *The MuSun Experiment*, PSI Proposal R-08-01 (2008).

[8] Fleming, D. G., Mikula, R. J., and Garner, D. M. *Phys. Rev. A* **26**, 2527–2544 Nov (1982).

[9] Engfer, R., Schneuwly, H., Vuilleumier, J., Walter, H., and Zehnder, A. *Atomic Data and Nuclear Data Tables* **14**(5-6), 509 – 597 (1974).

[10] Measday, D. F. *Phys. Rept.* **354**, 243–409 (2001).